

Modeling and CFD Analysis of Thermal storage phase change materials integrated in solar receivers

Politecnico di Torino

Faculty Of Engineering

College of Mechanical, Aerospace, Automotive and Production Engineering



**Politecnico
di Torino**

Ahmed Mohamed Elsbali

Supervisors: Prof. Massimo Santarelli
Prof. Davide Papurello

Decemebr 2021

Abstract

Micro Gas Turbine (MGT) device based on solar dishes have the potential to be fascinating small-scale power stations, in off-grid or mini-grid contexts for electricity as well as poly-generation production. The solar receiver which shall work at high temperature and concentrated sun radiant energy is by far the most challenging part of such arrangements. Consistency of thermal energy input to the MGT is the key factor since they are affected by temperature changes caused by the natural variations that occur in the solar flux. Nevertheless, to prevent this effect, a new generation of the solar receiver is suggested integrating with Phase Change Material (PCM). The proposed CSP system is located at the Energy Center (Turin), Italy. The geometry is shaped with a cylindrical confinement material included the PCM, and 12 tubes to make the fluid (Air) flow. In this discussion, we focused on an ideal design of the receiver depending on the desirable input variables. To evaluate beforehand the impact of several controlling parameters on the temperature, quantitative simulations have been done by using Comsol Multiphysics software in which a CFD approach is applied. Heat transfer through solids and fluids applied in our model to estimate the transmission of the heat along the tubes. The cavity dimensions, solar incident flux, air outlet, and hot wall temperatures are the criteria imposed in this study. According to MGT specifications, a group of PCMs has been shortlisted based on their suitable properties. These PCM's have a melting point of even more than 800 °C and a latent heat of fusion greater than 500 kJ/kg. we discussed the variation of temperature by imposing a time-dependent study with an appropriate time step, the targets period started from March to August.

Dedication

For only having people so great guarding my back, that I could dash forward without any concerns. Dedicated to my Parents Prof. Mohamed and Ruqayah.

Acknowledgements

I want to thank my supervisor professors Massimo Santarelli and Davide Paprulle, for all of their efforts and helping me countless times along the construction of this thesis, without them, it wouldn't come out as it is now. I would also like to thank the professors both in my country and here in Politecnico di Torino for the knowledge and skills I acquired during my time at the university. Finally, I thank my family and friends for their continuous support.

Abbreviations

CFD	computational Fluid Dynamic
MGT	Micro Gas Turbine
PCM	Phase Change Material
HTF	Heat Transfer Fluid
TES	Thermal Energy Storage
HTTES	High-Temperature Thermal Energy Storage
CSP	Concentrator Solar Power
SiC	Silicon Carbide
MgSi	Magnesium Silicade
NiSi	low density parity check
Mg2Si	channel state information
AlSb	Aluminium antimonide
DNI	Direct Normal irradiance
LHS	Latent Heat Stoarge
SHS	Sensible Heat Stoarge

Nomenclature

β_t	Expansion factor	[—]
β_c	Compression factor	[—]
γ	Specific heat ratio	[w/kg]
ε	Dissipation rate	[—]
ε_{sic}	Emissivity of SiC	[—]
ε_r	Regenerative exchanger efficiency	[—]
ε_{rs}	Solar receiver efficiency	[—]
η_{pi}	Hydraulic efficiency	[—]
$\eta_{optical}$	Optical efficiency	[—]
η_{MGT}	Micro-gas turbine efficiency	[—]
η_{is}	Isetropic efficiency	[—]
η_o	Organic efficiency	[—]
λ	Thermal conductivity	[$W/m.k$]
μ	Dynamic viscosity	[$Pa.s$]
ρ	Density	[kg/m^3]
ρ_R	SiC reflection coefficient	[—]
σ_B	Boltzmann constant	[$w/m^2.k^4$]
ϕ	Specific thermal power	[w/m^2]
ϕ_{conv}	Convection specific thermal power	[w/m^2]
ϕ_{irr}	Irradiance specific thermal power	[w/m^2]
$\phi_{re-irra}$	Re-irradiance specific thermal power	[w/m^2]
χ_l	Average lLiquid fraction	[—]
$\chi_{i,l}$	liquid fraction at a certain point	[—]
ω	Turbulent Frequency	[$1/s$]
h	Convection heat transfer coefficient	[$W/m^2.k$]
A	Heat exchange surface area	[m^2]
A_{dish}	Area of the dish	[m^2]
$A_{receiver}$	Area of the receiver	[m^2]
A_R	Turbulent Frequency	[m^2]
A_{ring}	Turbulent Frequency	[m^2]

A_{cav}	Area of the cavity	$[m^2]$
D	Dimater of the recievr	$[m]$
\dot{m}	Mass flow rate	$[kg/s]$
G	Irradince	$[w/m^2]$
l_f	Latent heat of fusion	$[J/kg]$
Re	Reynolds number	$[J/kg.k]$
Re_{tau}	Reynolds number in case of friction	$[-]$
Re_c	Theoretical maximum calculation speed	$[-]$
tt	Throught time	$[ss]$
t	time	$[s]$
T_m	Melting temperature	$[k]$
T_{PCM}	Phase change material temperature	$[k]$
T_{out}	Air outlet temperature	$[k]$
T_i	Air inlet temperature	$[k]$
T_{max}	Air maximum atemperature	$[k]$
U	Transmittance	$[w/m^2.k]$
u	Velocity	$[m/s]$
V	Volume	$[m^3]$

Contents

1	solar thermodynamics	5
1.1	CSP technology and global widespread	5
1.2	The development of solar power in Italy	6
1.3	Economic interests	7
1.4	Method of CSP Operation	8
1.5	solar power generation technologies	8
1.6	CSP Market	9
2	Storage Systems	13
2.1	The importance of a storage system	13
2.2	State of the Art	14
2.3	Thermochemical Process for high-temperature solar system	17
2.3.1	Thermochemical storage	17
2.3.2	Phase change heat storage	19
2.4	Encapsulated PCMs (EPCM's)	20
2.5	Heat pipes	21
2.6	Cascade PCM	21
3	Dish Micro-gas Turbine	22

3.1	Case Study	22
3.2	Receiver	23
3.2.1	Solar Receiver Geometry	23
3.2.2	PCM Material Selection for DMGTs	25
4	Modelling Solar Receiver By COMSOL Multiphysics	29
4.1	Geometric dimension	30
4.2	Material properties	32
4.2.1	MgSi metal alloy	32
4.2.2	Silicon Carbide	33
4.2.3	Air	34
4.3	Micro Turbo-gas	34
4.4	Physics inserted in the model	37
4.4.1	Heat Transmission	37
4.4.2	Turbulent Flow	42
5	Simulation and model result	48
5.1	Mesh Independence	48
5.2	Analytical formulation of the apparent specific heat	52
5.3	Daily Transient	54
5.4	Solution Inputs	54
5.5	Initial conditions	56
5.6	The months of summer and spring	59
5.7	Effect of Solar irradiance	64
5.8	Effect of changing PCM	69

5.9 Recommendations and Future Work	76
---	----

List of Tables

3.1	Geometric Dimensions of the Solar Receiver[29]	24
3.2	Properties of the PCMs materials used in simulation[30]	27
4.1	Properties of the PCM material used in simulation	33
4.2	Thermophysical Properties of Air	33
4.3	Thermophysical Properties of SiC [31]	34
4.4	Main characteristic in nominal design point	36
5.1	Types of mesh grid independence computed	49
5.2	Results of the Simulation in both cases of the Apparent specific heat	54
5.3	Results of the Simulation in both cases of the Apparent specific heat	59

List of Figures

1	Solar power tower concentrating light via 10,000 mirrored [3]	2
2	Solar steam engine for water pumping, near Los Angeles circa 1901[3]	3
1.1	Solar Energy Worldwide usage[6]	6
1.2	simplified scheme of CSP plant[7]	8
1.3	Solar Radiation Spectrum[11]	9
1.4	Types of CSP Technologies[9]	10
2.1	Active indirect concept for TES integration, two tank[19]	15
2.2	Scheme of the combined sensible and latent heat concept for thermal energy[19]	16
2.3	Six candidate thermochemical storage systems at temperatures of (300 – 1100 °C)[22]	18
3.1	Scheme of the solar receiver integrated with PCM storage system[28]	24
3.2	schematic details of Receiver geometry[29]	25
3.3	List of PCMs having the temperature range of 800–1300 centigrade and the latent heat of fusion greater than 500 kJ/Kg [29]	27
4.1	Solar Receiver Geometric Dimension in (mm)[28]	30
4.2	Selected Domain	32
4.3	DMGT Scheme [28]	35

4.4	Example of statistical simulation for the calculation of view factors	42
5.1	Finer mesh	50
5.2	Selected mesh	50
5.3	Zoom in zone of the air passage tube	51
5.4	Zoom in zone of the air passage tube	51
5.5	Variation of dashed specific heat with temperature	53
5.6	Variation of Gaussian specific heat with temperature	53
5.7	Energy Center data collected Represent the Radiation values changing with time	55
5.8	Lateral and upper cross section view	56
5.9	Inner view of the model geometry	56
5.10	Temperature distribution for the mesh selected	57
5.11	Liquid fraction contour for the mesh selected	58
5.12	Temperature distribution in case of more accurate mesh	58
5.13	Liquid fraction distribution in case of more accurate mesh	58
5.14	Average temperature of the PCM during the period of operation in the various months of the year	60
5.15	Average temperature of the Air outlet during the period of operation in the various months of the year	61
5.16	Liquid fraction of the PCM during the period of operation in the various months of the year	62
5.17	Maximum Temperature of the PCM during the period of operation in the various months of the year	63
5.18	Average wall Temperature of the PCM during the period of operation in the various months of the year	63

5.19	Effects of changing the radiation applied on PCM and Maximum Temperature achieved	65
5.20	Effect of solar radiation fluctuation on the outlet air temperature . .	66
5.21	Effect of solar radiation fluctuation on the average PCM temperature	67
5.22	Effect of solar radiation fluctuation on the Liquid Fraction	67
5.23	Effect of solar radiation fluctuation on the average wall temperature .	68
5.24	Effect of solar radiation fluctuation on the Maximum temperature . .	68
5.25	Temperature distribution profile for NiSi	69
5.26	Liquid fraction contour for NiSi	70
5.27	Temperature distribution profile for AlSb	70
5.28	Liquid fraction contour for AlSb	70
5.29	Comparison of the outlet air temperature by considering the selected PCMs during the radiation time	71
5.30	Comparison of the Liquid fraction by considering the selected PCMs during the radiation time	72
5.31	Comparison of the wall temperature by considering the selected PCMs during the radiation time	72

Introduction

One of the most controversial issues nowadays is related to the global energy challenges which are facing the world economy and modern lifestyle depending on the technologies powered by conventional energy sources depleting fossil fuel which can be burned for energy consumption. Expanding development is creating more demand for these resources, as a result, energy security climate change, and sustainable improvements are among the world's biggest challenges that can be addressed through a dramatic turn to renewable energy.

Current research is taking place trying to figure out the most effective methods to adopt the forms of energy such as wind, sunlight, geothermal and tidal waves, choosing which is the best solution for a certain application depends on several criteria. For example, wind energy is inexpensive, however, it is unreliable because of the intermittent nature of the wind and requires mechanical maintenance frequently, whereas geothermal energy depends on the location.

In the modern era, many countries started running behind sustainable energy due to the scarcity of non-renewable energy, consequently, solar energy is the most widespread renewable resource as it can be found anywhere the sun shines, compared with other green power sources, solar energy is easy to collect and use, and the total cost is relatively low. Although solar energy has the advantages of no pollution and low impact on the environment.

It can be derived through three different techniques: electrochemically, photochemical, and thermochemical. The solar electrochemical method is involved in water electrolysis for generating hydrogen and syngas where the electric power required for this process can be obtained through photovoltaic panels or solar thermal power plants.[1]

Concentrated solar power and also known as (CSP) systems, is one of those techniques used to produce electricity by using the reflecting radiation from the sun on a small cross-section surface at which the heat transfer fluid (HTF) temperature is increased to reach the vapor state. The Carnot Cycle limits the efficiency of the electricity generated by an electric generator operated by a steam turbine.[2]

Concentrating solar power (CSP) technologies are one of the renewable technologies that play a major role in solving the present and future electricity problems due to the usage of solar radiation. [2]



Figure 1: Solar power tower concentrating light via 10,000 mirrored [3]

Historically, a legend says that Archimedes has burnt a glass on a concentrated light reflected from the sun on the invading Roman fleet and repelled them in Syracuse, Sicily. In 1973, a Greek scientist, Dr. Ioannis Sakkas, wanted to know whether Archimedes could destroy the Roman fleet in 212 BC, nearly 60 Greek sailors lined up in a row, each holding a rectangular mirror to catch the sun's rays and pointing them at the 49 m away tarred plywood silhouette, but the procedure was not successful. Auguste Mouchout created the first solar steam engine in 1866, using a parabolic trough to produce steam. In 1886 an Italian inventor from Genoa created the first patent solar collector.[3]

Generally, there are four CSP technologies, namely parabolic trough technology where the pioneering system was built and exhibited in Maadi, Egypt in 1913, Linear Fresnel The prototype of the Fresnel collector was built in Genoa, Italy, in 1964; the prototype of the Stirling/dish system was demonstrated in Southern California between 1982 and 1985; and the first solar tower power appeared in Adrano, Sicily, Italy, in 1965 used plant constructure called EURELIOS to generate 1 MWe.[3]

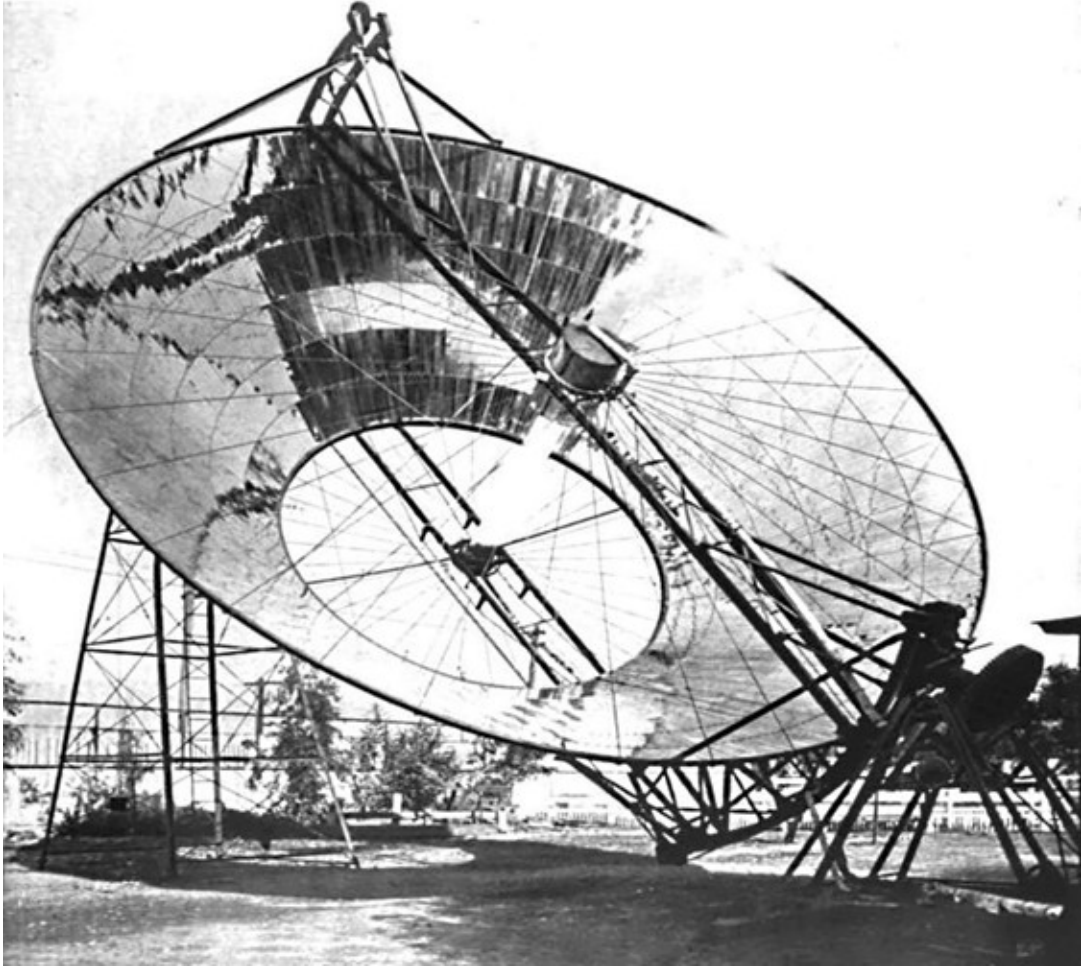


Figure 2: Solar steam engine for water pumping, near Los Angeles circa 1901[3]

From 1990 to 2005 there was no activity regarding the construction of solar thermal plants, but in 2006 the building of CSP plants has been steadily expanding due to the growing thermal efficiency and a capacity factor of these technologies. [4] China and the United Arab Emirates were the first to construct CSP; nevertheless, development, diversification, and geographic area are becoming increasingly encouraged, thanks to the rising cost of a unit of electricity produced. Several developing countries that have a high level of solar radiation such as India, Egypt, Morocco, and Mexico are moving to concentrate solar power for generating electricity.

The following chapters will deal with the hints which were mentioned above. Firstly, argues which are discussing the technologies of concentrating solar systems, following an overview of the thermal storage system analyzing the most evolution material provided to be used in this field. Nevertheless, specifications related to the receiver which is the most critical part of the solar system will be analyzed, a model will be constructed by using COMSOL multiphysics software to describe its operation method, some collected data from the Energy Research Center in Turin will be used to examine the device performance in different irradiance conditions.

Chapter 1

solar thermodynamics

1.1 CSP technology and global widespread

Solar energy is the most important source of renewable energy which is exploitable in the world, solar thermodynamic systems or CSP in addition to the photovoltaic systems are the best known for being the only energy technology capable of generating electricity, thanks to the radiation of the solar through the mirrors to reach to the temperature high enough to be able to feed the thermodynamic cycle.

Sensible heat storage is a possible way to store the thermal energy for CSP systems and it can be implemented by liquid or solid storage media, as well as the latent heat storage through phase change material (PCMs) in addition to thermochemical storage by reversible chemical reactions.

Several factors should be taken into consideration when designing a TES for CSP systems : (1) specific enthalpy drop in load and normal temperature. (2) maximum load and the strategy of operation. (3) inclusion in the power plant. (4) the storage of thermal system expenses.

Worldwide installation of CSP reached 5,500 MW in 2018 while it was about 354 MW in 2005, Spain is considered as one of the countries which have almost half of the globe's capacity by producing 2,300 MW, regardless of no new installation is done in the country since 2013, following that USA is the second with 1,700 MW, Middle East as well as North Africa beside India and chine have also attracted attention in this sector.

1.2 The development of solar power in Italy

Apart from the more conventional solar PV technology, Italy may in the future challenge Spain as the role of Europe's leading country in the developing technology concentrated solar power (CSP). Which requires more direct solar irradiation to function properly. However, the southern regions, as well as the islands of Sicily and Sardinia, are convenient conditions for CSP.[7]

Italian inventors like Giorgio Nebbia and Giovanni Francia have shown their interest in the solar power sector during the period of the oil shock in 1973, starting from 2000's Italy ranked the third following Germany and Spain in the solar power installations, this significant progress has been encouraged by a governmental plan called "Conto Energia" program which was initiated to enhance the green energy. In 2013, solar power accounted for 7% of all electricity generated in Italy, placing it the first in the globe, this figure at 8%, and more than 730 000 solar power plants installed in Italy and overall capacity exceeded 20 GW by 2018.[6]

There was a shift in policies following World War II. Energy demand was increasing dramatically, and new regulations targeted directly at supplying energy through imported fossil fuels and nuclear energy development. As a result of these changes, the country's reliance on imported fuels increased to more than 80% in 2005.[1] Italy is aiming to double the capacity of the project to reach approximately 30 GW in 2025, and that would increase the per capita ratio to 864 exceeding the EU expectations. However, the potential could be even higher, with a growing range of 1 GW/year. [1]

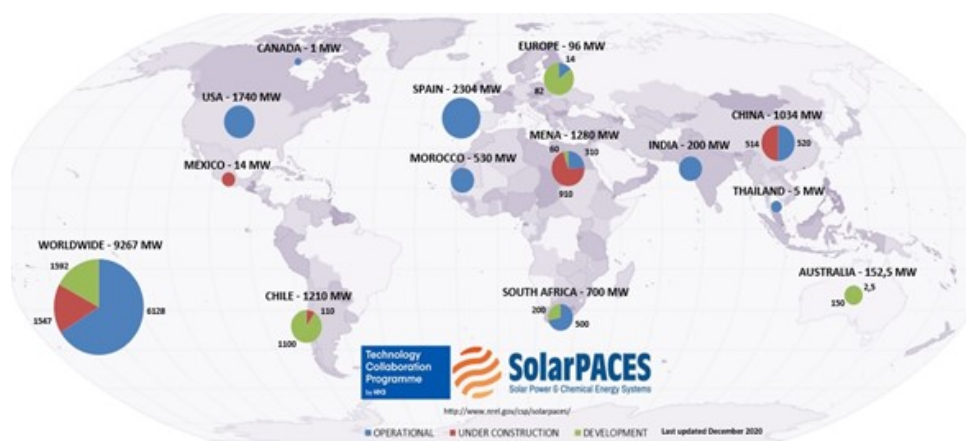


Figure 1.1: Solar Energy Worldwide usage[6]

In 2016, India, China, and South Africa were the top countries that have a major role in installation solar concentration plants producing an operational capacity of 100 MWe, forming a global capacity of 4,800 MWe by the end of the year.[7]

Nevertheless, in the last ten years, the annual increase in overall worldwide capacity has become the smallest. Considering the list of projects which are actively being built or developed (projects that have a signed agreement), In the coming years, a further 8,543 MW-hours-electric (MWe) will be added.[7]

1.3 Economic interests

Reducing the cost of the expanding clean energy can be done by adopting the CSP systems, in areas with a high concentration of irradiation such as the Middle East, northern and southern Africa, and many places around the globe, CSP combined with thermal energy storage give the possibility of reducing the cost of energy mix at a national level,by allowing the grid to absorb larger amounts of energy from cheap variable Renewables.[8]

Moreover, there are many reasons in making the market slow in adopting the approach of consuming solar energy, the radiation is dilute on earth compared with typical kinds of other sources such as fuel and nuclear making it difficult to collect and use effectively. When comparing the cost of using conventional resources to generate the same amount of power, solar energy will be prohibitively expensive.[2]

Solar power generation is supposed to achieve market acceptance due to its beneficial and environmentally friendly zero carbon emission and cost-free sunlight. the production of electricity by using solar energy has reached a maximum point to achieve grid cost parity with standard fossil fuel power plants.

In 2011, the energy association in the US funded a project called (sun shot) aimed to reduce the Levelized price of electricity produced by the CSP systems to less than \$0.06/kWh by 2020, with less than \$15/kWh for thermal storage and an energetic efficiency significantly larger than 95

1.4 Method of CSP Operation

The thermodynamic solar system generally is made up of two disciplines: solar field and power block, the solar field is mainly composed of many arrays which are set up in a certain way to form a module of the concentrator, as a result, a reflection of the sun's heat will be produced by mirrors to a point or line with an average medium temperature (400 – 550 °C) or even greater at about (600 - 1000 °C). [3]

CSP systems mainly consist of four parts: heliostat field or solar tower collector, power block, structure housing the reflector (mirror), absorber which directs the solar beam. [9] the heliostat field is the most promising technique to concentrate solar power available on the market because it has a high operating temperature. Its function is to reflect the solar radiation incidentally on a single region, then transfer it to the power block by the storage system, and the conversion from heat to electrical energy is used through Rankin thermodynamic cycle. [9] Concentrators are developed to position the reflecting surface at the desired position and angle at any given sunlit moment.[10]

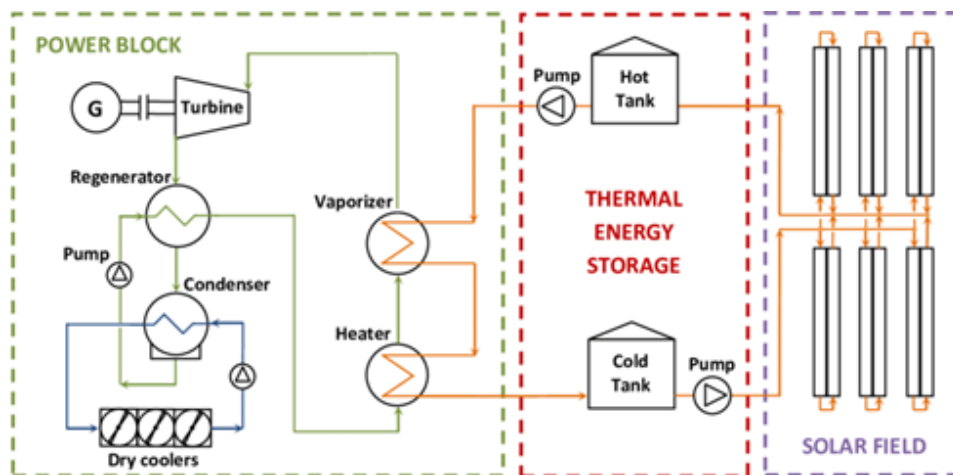


Figure 1.2: simplified scheme of CSP plant[7]

1.5 solar power generation technologies

The evolution of the dish is linked to power conversion as well as the receiver. The technology for concentrating solar power generation can be split into two broad categories: CSPV (concentrated solar photovoltaics) and CSTP (concentrated solar thermal power) are two types of concentrated solar energy.[11] Among which photovoltaic power generation technology is widely used. The photovoltaic effect is

used to transform the sunlight to electrical direct current. Photovoltaic materials are used to absorb sunlight, which contains photons of various wavelengths.[10]

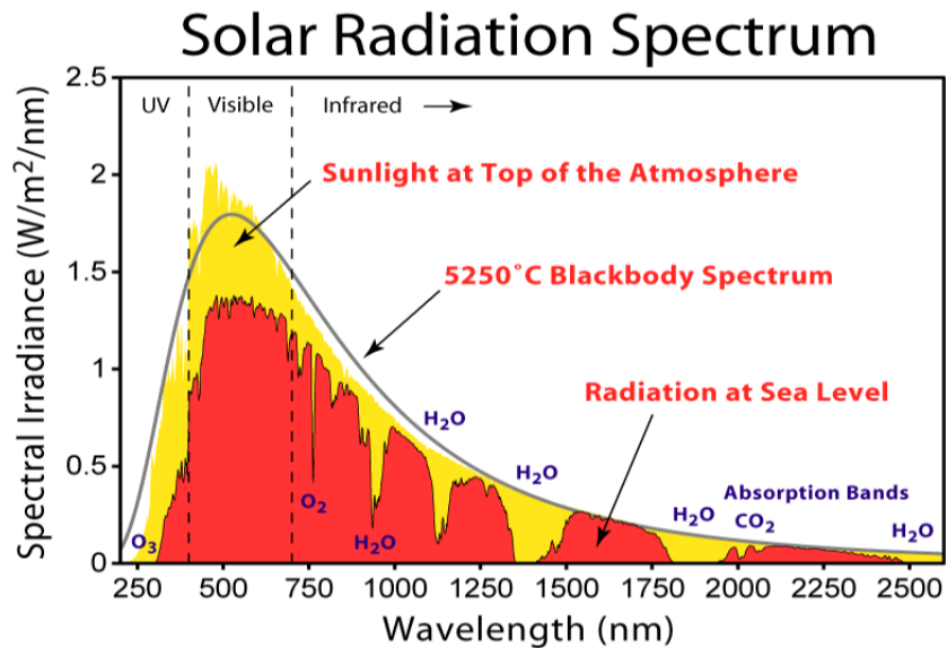


Figure 1.3: Solar Radiation Spectrum[11]

Photons having higher energy than the band gap can excite electrons in photovoltaic materials, causing them to jump out of the band gap and achieve a free-electron state.[10] It has been demonstrated that increasing sunshine concentration helps to improve solar cell efficiency and reduces the cost/efficiency ratio.

1.6 CSP Market

The study of sustainable energy and its practical applications has exploded in recent decades. Solar energy is one of the technologies that has received the greatest benefits from international commitments aimed at decreasing and limiting CO₂ emissions from energy storage systems.[7]

Several kinds of the possible system involving technological combinations are feasible, solar energy and fossil fuel co-firing plants are favorable, the reason is that they help to ensure a consistent peak-load supply even on cloudy days. [12]

CSP plants concentrate sunlight through the following methods:

- PTC (Parabolic Trough collector): It's a thermal collector with a polished metal mirror that is designed as straight in one dimension and curved like a parabola in the other two dimensions.
- SPT (Solar power tower) or receiver: also known as (Central tower), it uses flat array to focus the sunlight on a movable mirror. Among the four forms of CSP, it has the highest thermal–electric conversion efficiency.[13]
- LFR (Linear Fresnel Reflector), fixed receiver: small thin lens combined to simulate much thicker simple lens, the sun's energy can be concentrated to about 30 times its regular intensity using these mirrors. It's less expensive than other CSP systems but the heat–power efficiency is lower.
- PDC (Parabolic dish collector): systems use mirrors that are mounted over a parabolic-shaped dish to focus the sun's rays onto a receiver.

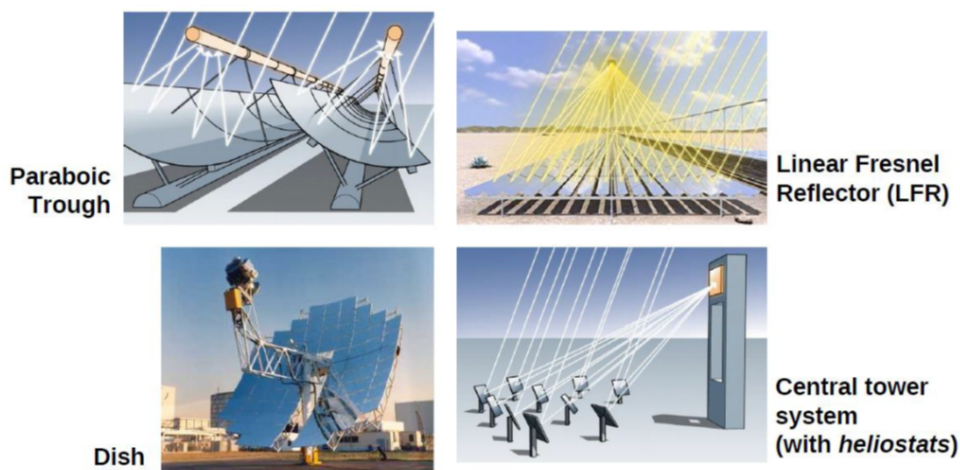


Figure 1.4: Types of CSP Technologies[9]

Solar power Towers are characterized by their capability to concentrate the radiation in a single point. Whereas the Parabolic Trough, as well as Linear Fresnel Reflector, are remarkable to control the effect of the radiation linearly. Although each of them has different aspects depending on the optical characteristics, costs and maximum temperature can be reached during the operation.[9] These conditions have a major role in deciding whether the system is appropriate or not for a certain application. SPT's and PDC's are the main prominent techniques in the market nowadays. SPT's cover about 80% of current power capacity, indicating the modern technology, with the lowest operational and economic problems.[14]

gaining the most attention is found in the biggest overall capacity of the plants under development, which is nearly double that of the PTC.[15] Generally speaking, it is possible that the initial investment expenses are solely concerned with the financial mechanism, but also possible to reduce the cost of the technology itself. Such a reduction may occur due to increased commercial adoption of these technologies, which affect economies of scale.[15]

CSP Market barriers

High initial capital expenditures, financial hazards, technology, and regulatory risks are all common obstacles to CSP commercialization, including the lack of present reference plants, cheap competing fuels, a dormant industry. For instance, energy market liberalization (e.g., shorter depreciation periods for power plant investments), additional barriers in developing nations, and high transaction costs. All barriers are known and manageable, however, there can be probably observed a cumulative effect of the single barriers.[16]

- Capital cost and finance: the highest barrier to commercializing CSP, according to most CSP publications and practically all interviewed CSP specialists, is the high capital cost compared to traditional fossil-fuel plants. The investment costs are typically 2,5 to 3,5 times greater in the short term for traditional plants. The higher initial capital cost is expected to be compensated by the savings in fuel costs and credits for carbon reductions during the operation.[17]

- Risks: Risks can be classified into two categories in the context of renewable energy technology: technology risks and regulatory risks. Uncertainties arise as a result of those concerns.
- Transaction costs: apart from the greater technological and construction costs of a CSP plant, there are several hidden costs associated with huge projects such as CSP plants. The costs of market transactions, or short transaction costs, have received a serious of attention in recent economic research.

Chapter 2

Storage Systems

2.1 The importance of a storage system

CSP combined with energy storage can deliver stable, scalable, and reliable power. Thermal storage allows solar heat to be stored during sunny periods and converted to energy afterward. As a result, thermal storage aids in the dispatchability of solar electricity, making it a reliable source of energy output.[18] As previously stated, the first issues that arise when discussing renewable energies such as solar and wind are their intermittency and imperfect predictability, which leads to energy generation that cannot be programmed. This will encourage technical and financial problems which in turn create a rapid penetration of these technologies.

Meanwhile, the grid's stability is affected by the intermittency of these sources, which makes it more difficult to maintain a balance between energy flows entering and leaving the grid. Local blackouts result from a lack of balance in the latter, which, if not controlled, can spread like wildfire and threaten the entire national grid.[9] Second, the daily variation of renewable energy sources does not mirror the needs of various consumers, severely limiting the value of the plant's capacity factor. which achieves substantially lower values than those obtained through the use of more conventional methods.

Lastly, because production is difficult to be scheduled, it is impossible to plan a period when it would be more convenient to sell this energy to improve the plant's economic return. The combination of renewable energy technologies with energy storage systems mitigates each of these issues, simplifying plant and power grid management and enhancing capacity factors by extending the production time slot [9]. In the case of thermodynamic solar systems, this connection results in an oversizing of the heliostat field in comparison to the power block. In this way the latter, not a negligible part of the total investment cost of the plant.

Therefore is better exploited going to the electric energy produced. This is only conceivable if the higher revenues received from the addition of an accumulation outweigh the additional cost, which, as predicted in the previous chapter, is always true in the case of lowering the cost of CSP plants for a wide range of accumulation capacity.

2.2 State of the Art

It is necessary to describe the current technological context of these types of systems in order to better explain the benefits and drawbacks of using PCM materials and to motivate the interest in that type of storage for HTTES (High-Temperature Thermal Energy Storage) systems. Like many other components, thermal storage systems could be categorized in a variety of ways. Firstly, the difference between active and passive systems, the former are distinguished by a storage medium that circulates in a heat exchanger and is further classified as direct and indirect [9].

Direct active storage tanks also use of HTF as a storage medium and are one of the most commonly installed configurations. The benefit is that there is no need for an intermediate heat exchanger, allowing for lower total efficiency. In contrast, indirect ones have a second means of storing heat and an intermediate heat exchanger between the two. The natural static of the storage system which is only sensitive to convective phenomena distinguishes passive thermal storage devices. The most important distinction, however, concerns the type of material used for heat storage.

The main TES (Thermal Energy Storage) technologies are grouped into three macro-categories depending on the heat storage material: sensible heat storage, latent heat storage, and thermochemical storage.[19]

2.2.1 Sensible Heat Storage

Reservoirs use this type of mechanism, known as SHS (Sensible Heat Storage), which are currently the most common and frequently used since they are quite simple and thus cost-effective. Specifically, a liquid substance SHS is used in 99.8% of installed capacity. [9] The characteristic technology that distinguishes this kind of storage consists in the constant phase process of the material used as a storage medium; in most cases liquid or solid phase to optimize the energy density value (Q/V) of the component.[19]

However, the heat storage capacity depends on the amount of "accumulating" material (in terms of mass or volume), its ability to store heat (expressed by the specific heat), and its allowable temperature jump, and is therefore calculated by the following equation:

$$Q = \int_{T_1}^{T_2} V \rho C dT \quad (2.1)$$

To ensure a high degree of energy density, the ideal material must have high specific heat and density values, as well as other physical-chemical properties, and thus be cost-effective.[8]

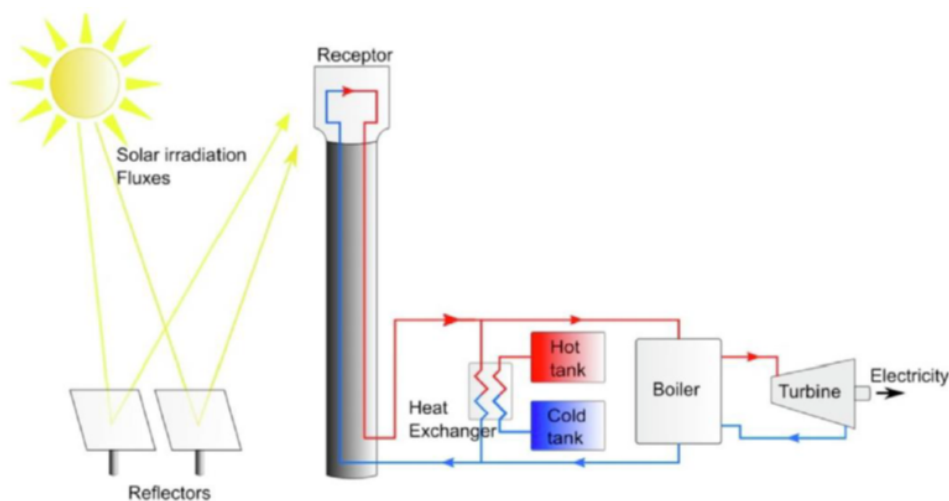


Figure 2.1: Active indirect concept for TES integration, two tank[19]

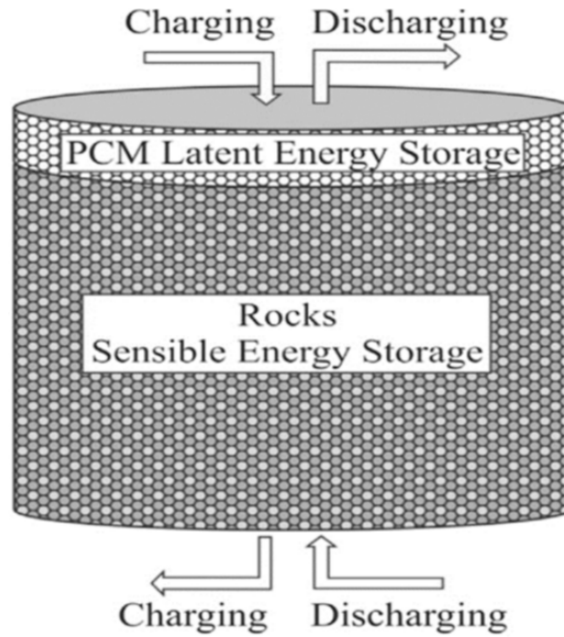


Figure 2.2: Scheme of the combined sensible and latent heat concept for thermal energy[19]

2.2.2 Latent heat storage

In latent heat storage, thermal energy is stored/released by material while changing its phase at a constant temperature. During charge or discharge, it is also a purely physical process with no chemical reactions. The latent heat of phase shift is usually the amount of heat stored (the latent heat of fusion for a solid-liquid transition and latent heat of vaporization for a liquid-vapor transition).[19] For latent heat storage, phase change materials (PCM) offer the benefit of being able to charge or discharge in a restricted temperature range, near their phase change temperature.[19]

The fundamental disadvantage of PCMs is their low thermal conductivity (about 0.2–0.8 W/m.k), which causes extremely slow charge and discharge operations. High thermal conductivity (about two orders of magnitude higher than molten salts) and good thermo-chemical stability are two advantages of PCMs composed of metal alloys (i.e. Mg- Zn-Al). Nevertheless, their high cost makes them unsuitable for large-scale TES. The melting point of these PCMs is typically between 100 °C and 900 °C. Materials with the lowest phase change temperatures (100–300 °C) could be utilized as PTC, LFR, and PDC TES systems.[19]

2.3 Thermochemical Process for high-temperature solar system

Solar thermochemical processes are represented in an indoor environment to examine the reactor performance as well as the dynamic of the process, this can be implemented by an approach known as high flux solar simulator (HFSS), this approach creates a concentrated solar energy source with a spectral distribution similar to the one comes from the sun.

Processes for producing fuels (hydrogen/ syngas) and industrial commodities can be categorized as solar thermo-chemical processes. Solar fuels such as hydrogen can be produced by solar thermolysis or in a thermochemical cycle, while syngas can be obtained by upgrading of carbonaceous feed or from carbon dioxide and water splitting in a thermochemical cycle. Solar thermolysis involves direct dissociation of water at elevated temperature (1900 – 4000°K) by using a heat process.[20]

Thermochemical cycles are a set of chemical reactions which dissolve water and carbon dioxide into hydrogen and carbon/carbon monoxide, respectively. Syngas can indeed be produced in a thermochemical cycle using water-carbon dioxide mixture as the net input.

2.3.1 Thermochemical storage

Thermochemical storage has a high energy density and little heat loss, making it a better alternative for long-term storage with a small storage capacity. At temperatures below 400 °C, the sorption process normally retains low and medium-grade heat, and the heat of reaction is frequently between 20 and 70 kJ/mol. The investigated processes include metal salts with water, ammonia, methanol, or methylammonia, and metal alloys with hydrogen.[21]

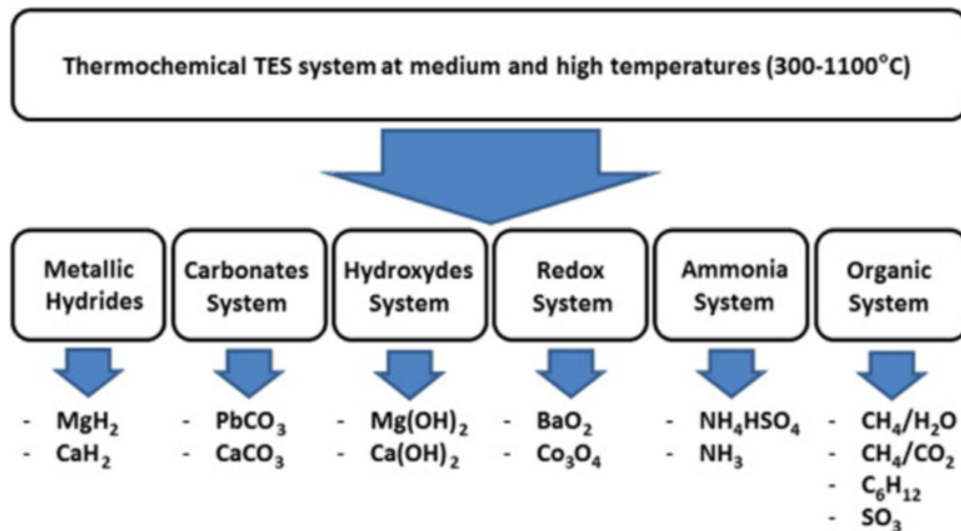


Figure 2.3: Six candidate thermochemical storage systems at temperatures of (300 – 1100 °C)[22]

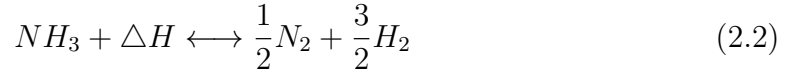
Pardo summarizes the various chemical processes that have been explored for possible thermal chemical storage plants, in which he illustrates the investigated thermochemical storage systems and the candidate reactants that are promising for CSP applications.

The volumetric energy density of thermochemical TES is 5–10 times larger than the volumetric energy density of latent and sensible TES.[22] In comparison to sensible and latent heat storage, thermochemical storage is at the first stage of the developing process and so far most of the systems are evaluated on a laboratory scale for a brief discharging period.

The volumetric energy density of thermochemical TES is 5–10 times larger than the volumetric energy density of latent and sensible TES.[22] In comparison to sensible and latent heat storage, thermochemical storage is at the first stage of the developing process and so far most of the systems are evaluated on a laboratory scale for a brief discharging period.

Generally, high temperatures are required to accumulate energy, but at the same time, much higher temperatures can be reached when this energy must be released. In addition, the energy density value obtained by these systems is the highest of all the types of thermal storage available today and since this energy is in the form of chemical potential energy, it can be stored indefinitely.

Chemical reactions utilizing metal/metal oxides and ammonia are currently the most important processes.[23] the following reaction equation is an example:



Many challenges face the future studies of thermochemical storage and they can be addressed as follow:

- One of the most appropriate chemical reactions should be chosen, and Wentworth and Chen's criterion should be followed.[24]
- Because mass and heat transport is poor, effective heat exchangers/reactors must be investigated.
- The development of innovative composite materials with high storage density, high thermal conductivity, proper cycle capability, and low cost is required.

2.3.2 Phase change heat storage

Past research on this kind of system, also known as LHS, has highlighted the potentially low cost of this kind of technology combined with an energy density value between 50-150 kWh/t. [23] much higher than classical molten salt sensible heat systems. The difference lies in the physical principle underlying their operation. PCM materials, used in the LHS, store energy through a phase change process that has the peculiarity to operate at a constant temperature as well as allow an exchange of energy per unit mass much more important than an SHS.

Following is the equation which is possible to calculate the heat exchanged by this type of storage:

$$Q = \int_{T_{min}}^{T_f} m_s c_s dT + L_f m_{cf} + \int_{T_f}^{T_{max}} m_l c_l dT \quad (2.3)$$

For an efficient implementation of the storage media, the phase change must match the operational temperature range. PCM materials can be divided into organic and inorganic compounds.

The organic materials are restricted at low temperatures, while the inorganic can maintain their performance at high temperatures and that is what makes them convenient for CSP storage applications. Because of their melting points and high energy density, carbonates, chlorides, and fluorides are appropriate examples that can be used. Yet, the PCM exhibits unfavorable corrosion behavior when acting with metals after a couple of thermal cycles. Several storage arrangements of LHS have been investigated. The combination between LHS and SHS will produce the sandwich concept system, on the other hand, the cascade system uses a variation of thermocline systems as well as melting temperatures.

2.4 Encapsulated PCMs (EPCM's)

In many cases, the PCM needs to be encapsulated to hold the liquid phase of PCM and also to avoid the PCM contact with the environment, the PCM can be packaged in tubes, pouches, spheres, panels, or other receptacles in case of building applications where the temperatures usually lower than 30 °C. [25] encapsulation improves the heat transfer between the fluid and the storage. Since it has a greater ratio of a heat exchanger to the enclosed volume the spherical shape is the most studied geometry. Several materials which are applicable for high-temperature applications such as steel, nickel, sodium silicate, silicon dioxide, calcium carbonate, and titanium dioxide have been specified as potential shell materials.

The EPCM can be manufactured by batch assemble and individually assemble. The single process in a batch assemble is a method of making several EPCMs, often they are small in size. Criteria such as the Core-to-shell ratio used to detect the mechanical strength of EPCM and affects the heat transfer performance of PCM. The preliminary cost estimation indicated that the TES system based on the developed PCM capsules can produce energy at a cost of USD 14/Wth.[25]

2.5 Heat pipes

A thermosiphon is an effective heat exchange approach that circulates a fluid without the necessity of a mechanical pump. As a result, the heat transfer between the PMC and HTF increases by combining it with embedded heat pipes. Which can properly transfer heat through condensation and evaporation utilizing an internal working fluid.

At the evaporator side of the heat pipe, the working fluid absorbs and turns into vapor and creates higher pressure. Because of the pressure difference, the vapor moves within the pipe to the condenser side and returns to the liquid state. Interestingly, a numerical model with varying complexity is used to investigate the behavior of the heat transfer of the heat pipe.

2.6 Cascade PCM

Using more than one PCM in a cascade configuration improves the rate of heat transfer of the storage system during the process of charging and discharging is taken place, several models including a variety of PCM systems are connected in series. In addition, the melting temperature diminishes in the charging process (PCM Melts), on the contrary, it rises in case of discharging process (PCM Solidifies). In a separate PCM system, the HTF temperature drops in the charging process along with the direction flow. It follows that a decrease in the heat flux and the heat transfer rate to the PCM, apart from this CSP plants are unable to deliver the needed nominal power output when the heat transfer rate falls below a particular threshold.

Although the temperature of the HTF drops in the flow direction during the charging process in a cascaded setup, the temperature differential between the PCM and the HTF can be kept nearly constant if the PCM is selected properly. As a result, the heat flux into the PCM is fairly constant, and the power production is considered stable. Moreover, Using numerous PCMs has many advantages, including increasing the heat transfer rate and achieving constant HTF outlet temperature. Which in turn increases the exergy performance and the effectiveness of extracting stored power.[25]

Chapter 3

Dish Micro-gas Turbine

3.1 Case Study

Solar paraboloids illustrate the concentrating solar technology which can reach the highest temperatures (higher than 1000°C). considering these temperature values they would lend themselves well to the coupling with any type of thermodynamic cycle but the short-term fluctuations of solar radiation that may occur during the daylight can generate technical issues which in turn will reduce the performance of some systems or, in the worst case, damage them.

In the case of DMGT (Dish-Micro Gas Turbine) systems, the continuous progress in the development of high-temperature phase-change materials offers today the possibility to design this kind of system to overcome such technical problems. Thermal storage of latent heat (LHS), properly integrated into the receiver, allows ensuring sufficient thermal inertia of this component to obtain as a result of a roughly constant output temperature even in the presence of fluctuations in solar irradiance.

Compared to conventional disc systems coupled to Stirling cycles, the latter has several complications that prevent their diffusion and it can be solved with a DMGT system, including:

- The use of heat transfer fluids which are difficult to be available (such as helium, hydrogen..etc); high internal pressures.

- Need for increasing maintenance due to a greater number of moving parts and, consequently, reduced system reliability.

In addition, micro turbo gas is also more compact and lightweight, thus facilitating installation of the component (whose costs are therefore lowered) and reducing the mechanical loads on the support resulting from the high weight of the component and the possible presence of wind. [27] Taking all this into account, several techno-economic analyses have highlighted how these systems can potentially be better performers than the classical disk system coupled to a Stirling cycle.

3.2 Receiver

The receiver in this case is the most complicated component since it has to be designed to guarantee heating ranging from 600 C to at least 800 °C while also having sufficient thermal inertia to prevent a rapid drop in the outlet air temperature in the presence of natural radiation fluctuations.[28] For this purpose, the phase change materials (PCM) installed directly on the receiver, to reduce losses due to dispersion, seem to be an effective solution. In particular, concerning other more conventional storage systems, they allow preserving roughly constant turbine inlet temperature even in the presence of solar radiation fluctuations, preventing the risk of structural damage to the MGT.

3.2.1 Solar Receiver Geometry

The possible geometries of a solar receiver are theoretically unlimited. The challenge lies in defining the optimal geometry design to best absorb the concentrated solar radiation while integrating the thermal storage system and improving as much as possible the heat exchange inside the component. To achieve this, a variety of geometries have been considered, starting from the simplest ones such as the one shown in Figure 3.1, consisting of a cylindrical container in which some U-shaped tubes are immersed in the PCM.[28]

The possible geometries of a solar receiver are theoretically infinite. The difficulty lies in defining the most suitable geometry to better absorb the concentrated solar irradiance while integrating the thermal storage system to provide as much as possible heat exchange inside the component.

To achieve the aforementioned, several geometries have been considered, starting from the simplest ones such as the one shown in Figure 3.1, consisting of a cylindrical container in which some U-shaped tubes are immersed in the PCM.

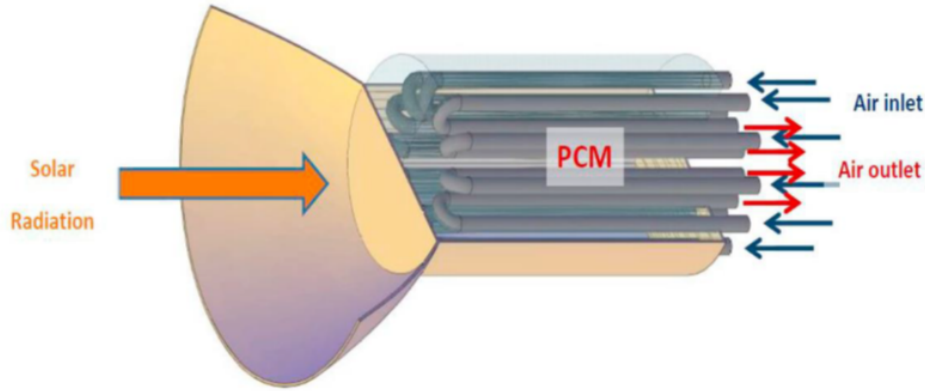


Figure 3.1: Scheme of the solar receiver integrated with PCM storage system[28]

Table 3.1: Geometric Dimensions of the Solar Receiver[29]

Receiver geometry	[mm]
Cylinder diameter	380
Cylinder length	440
Cavity diameter	180
Tube length	440
Tube diameter	19
No. of tubes	12

A numerical study was carried out, in which three different geometries of a cavity receiver: cylindrical, conical, and spherical in solar dish collectors were optically investigated. A conclusion revealed that the conical shape was the most benefits compared to the other two shapes.

Radiation heats the surface of the receiver, which is then transferred to the PCM, heat storage medium, and finally to the air moving inside the U-tubes. The hot outlet air can then be pumped into the turbine once this passage has been completed. The problem of this geometry is that, despite the good thermal capacity, the temperatures on the frontal surface of the receiver are too high to exceed the maximum temperatures allowed by the materials. Moreover, The liquid percentage is relatively low (about 60%) and the temperature gradients are extremely high.[9]

After evaluating the possible challenges and the importance of choosing an appropriate geometry, the research finished with the choice of the one illustrated in Figure 3.2, which was proposed and analyzed by Bashir and Giovanelli for a 10 kW DMGT system.[28]

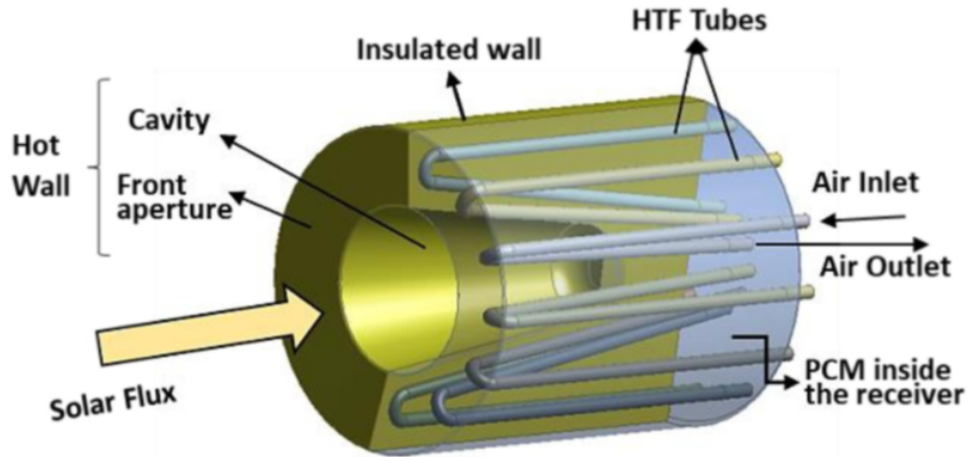


Figure 3.2: schematic details of Receiver geometry[29]

The device front (including cavity) and lateral surfaces, the PCM material, and compressed air movement inside the tubes are all considered in the receiver heat transfer model. The frontal cavity has the purpose to increase the absorbing surface of the concentrated solar radiation to reduce the temperature peaks and to reduce the radiation losses compensating for the largest share of losses in the receiver. The typical cavity ensures lower view factors, minimizing these losses significantly. Furthermore, it enables a wider exchange surface between the absorbent surface and the PCM material, thus improving the thermal exchange inside the component.

3.2.2 PCM Material Selection for DMGTs

There is a wide variety of phase change materials, each suitable for a certain temperature range that may be convenient depending on the application of interest. In particular, they can be classified into organic, inorganic, and their eutectics and blends. The purpose of defining the material selection is not to provide a comprehensive overview of all existing PCM materials only, but also to present those that can be used for systems operating at maximum temperatures. In other words, organic compounds are not suitable for CSP applications since they are not able to operate at high temperatures while inorganic salts, salt compounds, and metallic PCMs can be used instead.

The former constitute perhaps the most relevant and widely used branch of PCM materials for high-temperature applications. The main shortcomings are the reduced thermal conductivity, the corrosion phenomena that occur in contact with normal containment tank materials, and the large volume change that occurs during phase change. In particular, pure salts based on chlorides, sulfates, nitrates, and carbonates stand out from the dozens of existing inorganic salts because of their availability and low price.

These are also combinable in order to create salt compounds, usually binary or ternary, with better properties among which mostly chloride-based eutectic compounds stand out, which are characterized by high latent heat values and low cost[25]. However, various criteria, including thermophysical, chemical, ecological, and economic characteristics, must be considered when making choice. The following are the criteria that should be addressed while choosing a PCM material:

- Have melting temperature within the useful temperature range for the application of interest.
- High latent and specific heat values to increase energy storage capacity.
- Excellent thermal conductivity helps improve the efficiency of the charge and discharge operations by lowering temperature gradients inside the material and speeding up the phase change.
- Low-density variations to make the storage system technically more manageable.
- High cyclability (a large number of reversible phase change cycles).
- Being an abundant and economical material.
- It must be chemically compatible with the materials/fluids with which it interacts to sustain chemical stability.
- corrosion resistance, non-toxic, non-flammable, and non-explosive.
- reduced environmental impact.

According to Bashir and Giovanelli, a PCM material selection strategy for the case of the DMGT plant is shown below. A turbine inlet temperature of at least 800°C is required for this type of plant to be efficient and competitive. [29]

Furthermore, only materials with a latent heat value equal to or greater than 500 kJ/kg are chosen to achieve a high energy density, which is required to make the receiver more compact, hence limiting external environment losses.

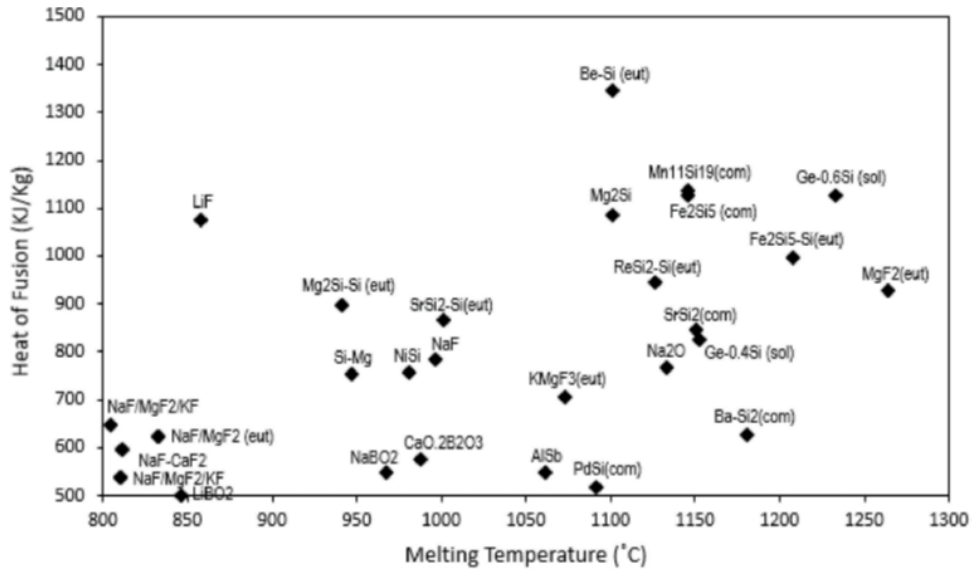


Figure 3.3: List of PCMs having the temperature range of 800–1300 centigrade and the latent heat of fusion greater than 500 kJ/Kg [29]

Another aspect to be considered is the need to speed up as much as possible the dynamics of the charging and discharging phases of the thermal storage so that the latter is able to handle the rapid fluctuations of solar energy that may occur during the day. which have conductivity values too low to meet this need.

The information offered is based on what is currently accessible in the literature, and it is still incomplete because not all of the properties of the materials listed in the table are known. Moreover, there are expensive materials such as Germanium (Ge), Strontium (Sr), and Rhenium (Re), or potentially toxic as Palladium (Pd). Taking into account what has been said, therefore, the potentially usable PCMs of which we know all the characteristics are 4:

Table 3.2: Properties of the PCMs materials used in simulation[30]

Material	MgSi(44%56)	Mg_2Si	NiSi	AlSb
Melting Temperature °C	946	1100	980	1060
Density (kg/m^3)	1900	1885	4833	4248
Specific heat [C_p] ($kJ/kg.k$)	632	1030	319	312
Heat of fusion (kJ/kg)	757	1090	760	420

Each of them has benefits and drawbacks. For E.g. Mg Si possesses high values of specific heat and latent heat of fusion but has the lowest thermal conductivity. NiSi and MgSi (44/56% by weight) have the maximum thermal conductivity ranges and the lowest melting temperatures near 800°C. AISb and NiSi have the best values of volumetric heat capacity and therefore compactness.[9]

However, Bashir and Giovanelli found that MgSi (44/56 wt%) had a higher ability to keep a consistent temperature for a longer time when starting from a fully molten condition. In figure 3.4 represents the results of the thermal storage discharge process including in each one of those four materials. In fact, It is notable how the thermal behavior of MgSi leads to better results, and for this reason, the latter material will be used in the following simulations.[29]

Chapter 4

Modelling Solar Receiver By COMSOL Multiphysics

COMSOL Multiphysics is a commercial software able to carry out analysis of different types and is useful in technological fields, ranging from industry to research. As a result, it's software that works effectively in a variety of situations and provides a wide range of computational approaches which are useful for solving various physical problems characterized by approximations and computational burdens more or less relevant depending on the objectives that are set. Electromagnetism, structural mechanics, acoustics, fluid dynamics, heat transfer, and chemistry are all disciplines of physics.

Thanks to the ability to create multi-physics models, any of these can be investigated separately or in combination with others, allowing almost any device to be modeled without restrictions. Therefore, it adopts well CFD analysis with great precision. That would suggest having a better combination of the laminar and turbulent fluid flow but with heat transfer problems. Among the common software such as ANSYS Fluent, StarCCM+, and ANSYS CFX, COMSOL is one of the most widely used software to perform this kind of analysis. The procedure of modeling begins with the definition of the component's geometry and then progresses to the specification of material properties. In addition, the physics of interest (conditions to the contour to be studied), the calculation domain (Mesh), and finally the style of research to be conducted (stationary or transitory).

In the following paragraphs, we'll go over each of these elements in depth in order to reconstruct the logical process which led to the establishment of the model which then will be applied in the simulations. Particularly focusing on different techniques implemented which give the possibility to reduce computational time while maintaining an adequate level of accuracy.

4.1 Geometric dimension

The geometry of the receiver has been described previously deriving from an optimization carried out by Bashir and Giovanelli.

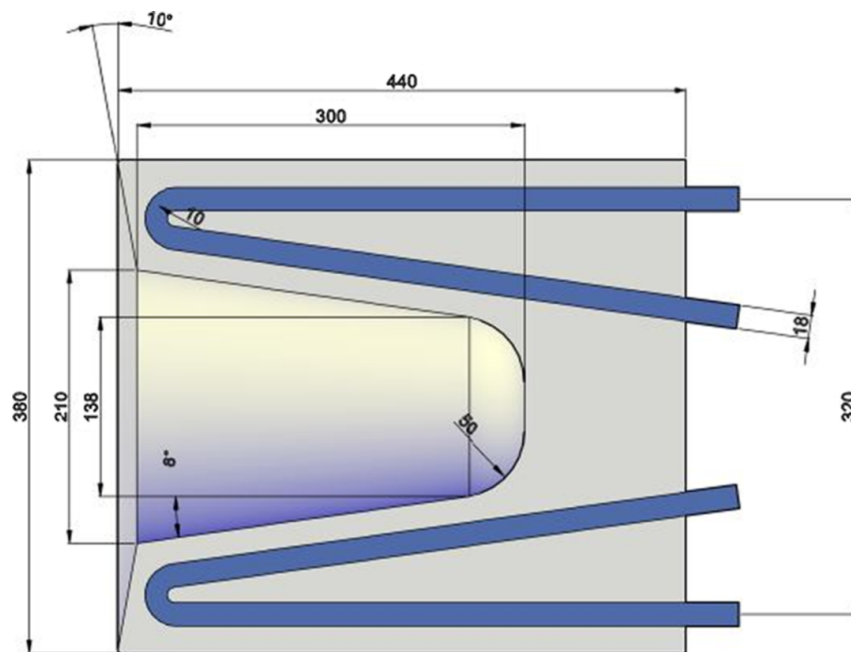


Figure 4.1: Solar Receiver Geometric Dimension in (mm)[28]

The volume of PCM contained in this sketch is approximately 41 liters, and it was computed using a thermal power extraction of around 32.5 kW. The value is included in an optimal range (around 30 to 35 kW) in order to feed micro turbo gas of 10 kW and 30 mins of storage time and that would be enough time to cover rapid oscillation of irradiance daily motion of the clouds. Taking into account the PCM type MgSi (44/56% wt) the calculation would be as follow:

$$PCM\text{volume} = \frac{\text{Thermal extracted power} \times \text{storage time}}{\rho l_f} \quad (4.1)$$

$$PCM\text{volume} = \frac{32.5[kw] \times 30[min] \times 60[\frac{S}{min}]}{1900 \times 757[\frac{kJ}{kg}]} = 41 \times 10^{-3}m^3 = 41 l$$

It's worth noting that the quoted geometric dimensions only include the tubes and the phase change material in which they are submerged, and not the exterior container. SiC was chosen as a containment material after reviewing the literature due to its outstanding thermophysical and structural features, chemical compatibility with MgSi, and high maximum operating temperature (it can work at very maximum temperatures up to 1600°C).

To consider the whole system as well as the geometrical dimensions, a containment reservoir with a thickness of about 5 mm is required, this reservoir must be strong enough and sufficient to withstand the expected mechanical stresses which may be subjected by the device even if it's thin and not contributing to creating an excessive thermal resistance for the heat flow entering the receiver.

Although the introduction of this thermal resistance is unavoidable, it should be emphasized that the usage of this reservoir has thermal benefits as well. The installation of this container increases the heat exchange inside the component, helping the homogeneity of the temperature inside the PCM, thanks to the high thermal conductivity of SiC which is roughly 120 W/m k. In addition, except for the frontal circular swath and the cavity, all other surfaces are covered with insulating material to decrease temperature losses to the outside as much as feasible.

Decreasing the computational domain as much as possible before implementing the geometry of the component on COMSOL is a technique which will be useful to lower the computer's computational cost. Since the tubes immersed in the PCM have different symmetry axes for the outer cylinder and the cavity, it was possible to adopt an axisymmetric 2D model while the choice was to work on a three-dimensional subdomain of the receiver constituting a "slice" of the latter equal to 1/24 of the entire volume. A representation of the new geometry thus obtained is shown in Figure 3.1.

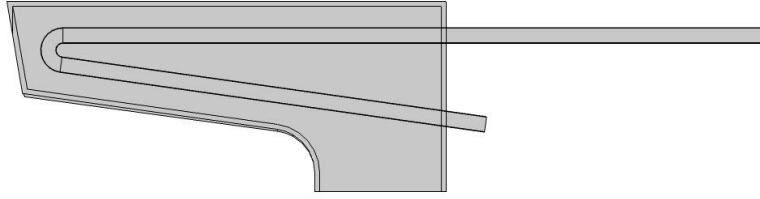


Figure 4.2: Selected Domain

To be precise, if the buoyancy effects of the air present, particularly inside the absorbing cavity, are taken into consideration, this choice of a domain would not be fully correct, resulting in non-symmetrical temperature distribution. Because the mixing phenomena that occur inside the cavity make the temperature of the air inside homogeneous, previous more detailed analyses have shown that this effect is negligible, so this simplified analysis should produce results that are well representative of reality at much lower computational cost because it is carried out on a domain with significantly less computation.

4.2 Material properties

MgSi alloy (the phase change material chosen), silicon carbide (SiC, a ceramic substance that makes up the inner tubes), and air are the three main components used in the model (i.e., the heat transfer fluid).

4.2.1 MgSi metal alloy

As previously stated, the MgSi alloy was chosen for its strong thermophysical properties, which allow for good thermal performance as well as a high level of energy density and hence component compactness.

Furthermore, the properties of this alloy have been assumed to be constant in both phases (liquid and solid) in which its function during plant operation, based on the little amount of data available in the literature on the issue. However, based on data from other high-temperature PCM materials, this idea appears to be quite valid, since the percentage variations of the properties of these materials are generally quite low.

Table 4.1: Properties of the PCM material used in simulation

Material	MgSi(44%56)
Melting Temperature °C	946
Density (kg/m^3)	1900
Specific heat [Cp] ($kJ/kg.k$)	632
Heat of fusion (kJ/kg)	757

Regarding the physics of phase change, the apparent heat capacity method, which consists of a temperature-dependent formulation of specific heat that inherently contains information about the latent heat of the material, is probably to be explored.

4.2.2 Silicon Carbide

SiC, or silicon carbide, is a fantastic choice since it bears high temperatures while keeping its mechanical properties, making it ideal for tube material. Another significant benefit is that it is chemically stable even at high operating temperatures, reducing the possibility of corrosive phenomena caused by contact with the MgSi metal alloy.

Table 4.2: Thermophysical Properties of Air

Material	SiC
Melting Temperature °C	1600
Density (kg/m^3)	3100
Specific heat [Cp] ($kJ/kg.k$)	750
Thermal Conductivity ($W/m.k$)	125
Emissivity ε	0.9

4.2.3 Air

The operating fluid in turbo gas is basically air, which has the advantage of being free and readily available. However, for the sake of this analysis, it will be treated as an ideal gas in order to simplify the model complexity, making it easier to implement and reducing the relative calculation times to the numerical resolution of the problem.

Table 4.3: Thermophysical Properties of SiC [31]

Working Fluid	Air
Dynamic Viscosity	$43.1 e^{-6}$
Density (kg/m^3)	1.208
Specific heat [Cp] ($J/kg.k$)	1004.5
Thermal Conductivity ($W/m.k$)	0.0716
Specific Gas Constant [R] ($J/kg.k$)	287

4.3 Micro Turbo-gas

As can be seen from the DMGT scheme, it consists of a solar disk concentrator coupled to micro turbo gas. In comparison to more traditional turbo gas, the latter works at lower power, lower compression ratios, and uses a regenerative Brayton-Joule cycle.

The recuperator R is meant to pre-heat the compressed air outflowing from the compressor C to exploit within the limit of the principle of the second law of thermodynamics, the outlet hot gases from the turbine T enhancing the total efficiency of the plant. The gas enters the solar receiver SR coming from the heat recuperator's outlet, in this case, SR is positioned instead of the classical combustion chamber of a conventional Micro gas turbine system. The pressure air heated up to around 800-950°C before entering the turbine, where it expands and spins the shaft connecting the compressor and turbine. [8] Eventually, the alternator turns the mechanical energy generated into usable electrical energy.

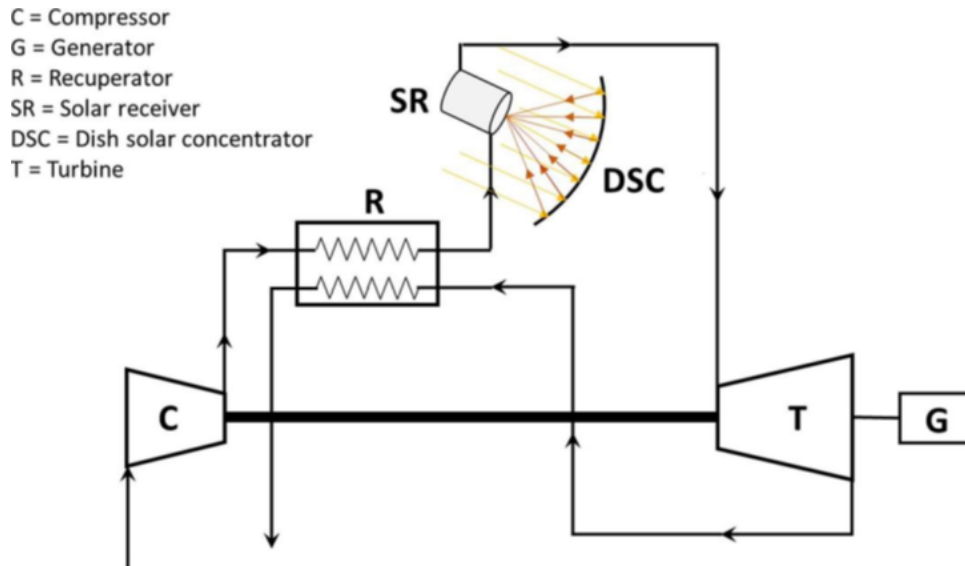


Figure 4.3: DMGT Scheme [28]

Among the most generally used forms of the plant at the moment includes an integrative combustion chamber with a certain temperature downstream of the solar receiver, with the function of further heating no longer constrained to the strength of solar radiation. In this case, we'll discuss hybrid DMGT systems, which have three major benefits:

1. Being independent of solar irradiance changes and the presence of the Sun, resulting in a significant improvement in capacity factor when compared to the integrative combustion chamber.
2. Achieve higher conversion efficiencies, allowing for better solar resource utilization.
3. Reduce the LCOE making the system more competitive.

In the case of hybrid systems, in addition to utilizing the solar source, fossil fuels would be used to feed the combustion chamber, resulting in a certain level of pollutant emissions. To avoid the abovementioned, we will not use hybrid DMGTs in this research. Instead, we will seek to get good outcomes by relying solely on solar energy, avoiding any pollution emissions into the atmosphere.

It was discovered that no practical MGT unit with polytropic turbine efficiency of more than 80% could be designed. Starting with a practical design that achieves the highest polytropic turbine efficiency of 80% and a pressure ratio of 3:1, a variety of design points that can achieve similar or greater conversion efficiencies were investigated.

Although the fact that interesting concepts were identified, no single-stage MGT unit could be constructed to meet the design requirements while also providing higher conversion efficiencies than the original design. The key characteristics of the ‘ideal’ design are listed in Table 3.2.

Table 4.4: Main characteristic in nominal design point

Feature	Value	Unit
Pressure ratio π	3	[-]
Engine speed n	95500	[rpm]
Total nominal conversion efficiency	29.6	[%]
Isentropic compressor efficiency $\eta_{is,c}$	η_{conv}	
Isentropic compressor	81.94	[%]
Isentropic turbine efficiency $\eta_{is,c}$	83.77	[%]
Isentropic turbine		
Air mass flow rate \dot{m}	0.2335	[kg/s]

Adopting the ideal gas model for air, with the specific heat capacity value 1.0045 (kJ/kg.K), and specific heat ratio γ equal to 1.40 from these assumptions we can combine the following equations to obtain respectively the values of work in case of expansion (l_t), in case of compression (l_c), the amount of heat absorbed (q_1) and the efficiency of turbo gas:

$$l_t = Cp T_4 \eta_{is,t} \left(1 - \frac{1}{\beta t^{\frac{\gamma-1}{\gamma}}} \right) \quad (4.2)$$

$$l_c = \frac{Cp T_1}{\eta_{is,c}} \left(\beta c^{\frac{\gamma-1}{\gamma}} \right) - 1 \quad (4.3)$$

$$q_1 = Cp (T_4 - T_3) \quad (4.4)$$

where βt and βc are correlated by the following equation:

$$\beta t = \beta c \eta_{\pi} \quad (4.5)$$

4.4 Physics inserted in the model

For simulation purposes, the complete geometry was decomposed into four domains of which three were solid and one was fluid. Mainly, the PCM material of the pipe and confinement parts are all solid domains. The fluid domain is inside the tubes where air flows through turbines. This subdivision is fundamental, the reason is that one of the previously mentioned domains is associated with the respective material, whereas, the type of domain (fluid or solid) depends on the instantly associated physics. Precisely, the physics of the case concerns the following:

- Heat Transfer is applied to the entire geometry using two different differential equations depending on whether the domain is solid or fluid.
- Turbulent flow (applied only to the fluid domain).

4.4.1 Heat Transmission

The differential terms used to model heat transfer phenomena are derived from the principle of conservation of energy. In the solid domains, the mathematical model is dominated only by the conductive heat transfer while in the case of the model used for HTF (Heat Transfer Fluid). Another point that would be added is that it focuses on the term of advective transport related to the field of fluid motion, the type of the domain also affects the way of deriving both the conservative and non-conservative differential equations as follow:

- The conservative form is utilized in the case of heat transfer fluid to consider the spatial-temporal gradients of its thermophysical properties.

$$\frac{\partial}{\partial t} (\rho C_p T) + \nabla (u \rho C_p T) = \nabla (\lambda \nabla T) \quad (4.6)$$

Regarding the heat transfer in PCM, the pipe, and the materials of the holding tank component the aforementioned equation is simplified using a non-conservative form. Apparently, it uses the heat capacity method, and that is the reason it's called the Partial equation. However, while thermal conductivity and density are considered constant in both time and space, the specific heat remains within the partial derivative calculated concerning time.

$$\rho \frac{\partial}{\partial t} (CT) = \lambda \nabla^2 T \quad (4.7)$$

Thunderstorms are relevant only for research during transient conditions, hence, they are excluded from analysis under stationary conditions. These equations in combination with the equations expressing the principles of conservation of mass and momentum, which will be discussed in part in the next paragraph, allow them to calculate the temperature and velocity fields at every point of the domain and each instant of time.

- All the surfaces of the complete geometry are not in direct contact with solar radiation, however, they are considered well insulated by imposing on them a thermal flux equal to zero (adiabatic condition or Neumann condition with zero thermal flux imposed).

The boundary conditions inserted in the model useful to obtain such results are the following:

$$-\lambda \frac{\partial t}{\partial n} = 0 \quad (4.8)$$

- The same condition expressed in the previous point is imposed on the remaining surfaces of the reduced geometry (i.e. the one with a volume equal to 1/24 of the whole volume of complete geometry described in paragraph 4.2), excluding only those in direct contact with solar radiation, to impose the condition of thermal field symmetry.

- Similarly, the aforementioned is applicable for the outlet section of the tubes through which the air passes, whose temperature is assumed to be independent of what is present immediately beyond that section.
- Instead, a continuous temperature condition (Dirichlet condition) of 590 °C is established in the inlet section.

The temperature of the air leaving the regenerative exchanger is an indication of its temperature (whose derivation is explained in paragraph 3)

$$T_{inlet} = 590 \text{ celsius} \quad (4.9)$$

The circular corona present on the frontal surface of the receiver (generally known as the solar ring), there are three kinds of heat flow are considered, one entering and two exiting, the existing flow is given by the convective heat exchange with external air (Robin condition). The convection coefficient is estimated to be 25 (W/m^2k), with an ambient temperature being constant at 15 °C.[33]

$$\varphi_{conv} = h (T_i - T_{ambient}) \left[\frac{W}{m^2} \right] \quad (4.10)$$

The second equation is provided by the re-irradiation losses towards the exterior environment, the flux is computed by the Boltzmann equation considering a value of emissivity equal to 0.9.[8]

$$\varphi_{re-irr} = \sigma_B \varepsilon (T_i^4 - T_{ambient}^4) \left[\frac{W}{m^2} \right] \quad (4.11)$$

Finally, the third sort of flux arises from concentrated solar radiation impacting the solar ring, which may also be characterized using the Neumann condition once again. Therefore, its value is determined by the solar radiation impacting the solar paraboloid, and on the optical characteristics of the latter as well as the receiver.

$$\varphi_{irr} = G \frac{A_{dish}}{A_{receiver}} \eta_{optical} (1 - \rho_r) \left[\frac{W}{m^2} \right] \quad (4.12)$$

With a reflection coefficient of 94% and an active area of $60(m^2)$, the solar paraboloid is considered high-performance. With a total A_{dish} area of $63.4(m^2)$, the optical efficiency of 88.96% can be calculated. The receiving area $A_{receiver}$ is considered equal to the surface of a circle with a diameter equal to that of the receiver, i.e. equal to 390 mm (since the thickness of the outer case is also considered). Ultimately, the reflection coefficient of silicon-carbide ρ_r is fixed at 10%. Rearrange the previous equations, we would obtain the resulting flux as follow:

$$\varphi_{tot} = \varphi_{irr} - \varphi_{conv} - \varphi_{re-irr} \quad (4.13)$$

The same factors that apply to the solar ring apply to the cavity, but with several important modifications. It is expected that the DMGT system in concern will only become operational if a high level of solar irradiation is achieved, which is now only possible in the morning. This means that the angle of inclination of the paraboloid and the receiver will be large enough to facilitate the stagnation of the air inside the cavity. Convection losses inside the cavity are considered negligible, due to the high internal air temperature values obtained throughout the DMGT working period.

However, in the case of the other two types of losses the concept of sight factors must be introduced. The cavity has the significant benefit of lowering the fraction of solid angle through hot external surfaces. The main heat sink where losses by re-irradiation and reflection are concentrated. Given the low value of ρ_r and introducing the concept of view factors, the reflection losses become insignificant. Consequently, The total losses in case of re-irradiance would become as follow:

$$\varphi_{re-irr} = GF_{i,ambient} \sigma_b \varepsilon_{sic} (T_i^4 - T_{ambient}^4) \left[\frac{W}{m^2} \right] \quad (4.14)$$

The view factor $F_{ambient}$ determined using the Monte Carlo approach in a simulation created expressly for this project. More precisely since we have three different geometries make up the cavity (truncated cone with a flat bottom and then we inserted spherical fitting), so we have to use three different correlations were obtained depending on the shape of the geometry used to build up the cavity and could be solved by several methods such as EXCEL and MATLAB.

Choosing the four-degree equation polynomial for the first section of the cavity and the polynomial second-degree equation for the second section. By running the MATLAB code in Appendix A for the flat bottom refers to a single view factor value of 6.35%, which is the same as the latest result obtained for the spherical fitting.

$$F_{ambient} = 0.0635$$

The correlation is, therefore, the following:

- for the truncated cone :

$$F_{ambient} = Ay^4 + By^3 + Cy^2 + Dy + E [R^2 = 0.9998]$$

where:

- $A = 187,874942645896 (m^{-4})$
- $B = 141,773300366267 (m^{-3})$
- $C = 42,7691714794642 (m^{-2})$
- $6,96307419003821 (m^{-1})$
- $0,618986033697146$

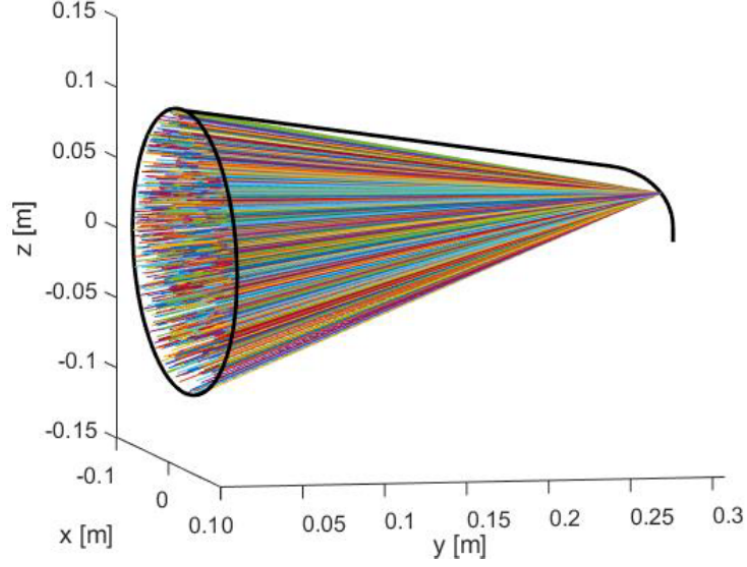


Figure 4.4: Example of statistical simulation for the calculation of view factors

The analytical simulation did not reveal significant differences as a function of reference height, hence, it was assumed to be constant all over the geometry.

4.4.2 Turbulent Flow

The overall heat absorbed from the PCM is influenced by the mass flow rate of air inside the tubes. The air within the tubes circulates at a high mass flow rate, absorbing more heat energy from the tube walls. The state of the air in the receiver is determined by several factors, including the Nusselt Number and Reynolds Number. However, in this case, we will use the Reynolds Number because we have the dimensions of the tube known and also the properties of the air which are already mentioned.

Considering Air inlet temperature $590\text{ }^{\circ}\text{C}$ and Air flowing rate at 0.1 (Kg/s) divided with a tube diameter of 18 mm , substituting in the Reynolds number equation we will get the following result:

$$R_e = \frac{\rho u D}{\mu} = \frac{4\dot{m}\mu}{D\pi} \quad (4.15)$$

$$R_e = \frac{4 \times \frac{0.1}{12} \times 3.846 \times 10^{-5}}{\pi \times 0.018} \quad R_e = 15326.64 \gg 4000$$

Therefore, the flow of the air is turbulent.

Additionally, because the airflow at the receiver inlet traveled from a long path which has been seen in graph 3.5 (passing the compressor and the regenerative exchanger). Hence it has been assumed that the air flow is under fully developed turbulent conditions. The given length of the pipe section has been inserted in the designing sequence in the software as a function of Reynolds number and the diameter of the tube by the following correlation[33]:

$$l_e = 4.4 (R_e)^{\frac{1}{6}} D \quad (4.16)$$

The turbulence model was then chosen as it can approximate the real behavior of a fluid. It avoids the use of direct simulations. In addition, the flow field would be obtained employing the various equations of continuity, momentum, and conservation of energy. The following equations of conservation of energy are applicable in the case of non-isothermal flow.

$$\frac{\partial \rho}{\partial t} + \frac{\partial}{\partial x_j} (\rho u_j) = 0 \quad (4.17)$$

$$\frac{\partial}{\partial t} (\rho u_j) + \frac{\partial}{\partial x_j} (\rho u_i \rho u_i) = - \frac{\partial p}{\partial x_i} + \frac{\partial}{\partial x_j} \left[\mu \left(\frac{\partial u_i}{\partial x_i} + \frac{\partial u_j}{\partial x_j} \right) \right] \quad (4.18)$$

The reason behind taking a long time for the simulation to run is that it directly solves these equations. Because the large space-time resolution needed to sufficient to transfer the mechanical energy transfer at the largest scales, which is known as the turbulence integral scale. Concerning that, an estimation equation to compute (through time tt) and it's used in the case of basic geometry, i.e. parallel plate channel.

Where:

- Re_τ is the frictional Reynold number, given that $Re_\tau = 100$ is roughly equivalent to $Re \approx 8000$, Re_τ will be nearly equal to 227 in case if Re is equal to the previously estimated value.
- χRe_c for a computer in 2014, it is the actual speed of computation of a machine stated in many floating-point operations per second (flops) (roughly corresponding to the year of purchase of the computer used for this study), we will assume that is equal to 2 Glops.

Using the previously mentioned numbers to calculate the throughout time tt the results would be around $2.33 \cdot 10^{16}$ seconds and if we convert to the days it will be nearly 270 days. For these reasons, and because direct simulations have exaggerated calculation durations (which can only be reduced to tolerable levels using supercomputers and only for very basic geometries), turbulence models have been used for years.

which theoretically develops the Navier-Stokes equations in estimating the fluid performance with that of an equivalent fluid that exhibits a suitably regular and predictable space-time behavior under the same conditions[33] and closely approximates the real behavior of the fluid. In addition, LES (Large Eddy Simulation) and RANS (Reynolds Averaged Navier Stokes) are simulation methods considered as two macro-categories based on spatial and temporal filtering respectively.

The spatial filtering performed by LES is based on the idea that higher scale structures have more information such as large vortices, which are primarily responsible for convective transport, momentum, and turbulent energy, which makes it not applicable for the modeling.

The reason is that they must be explicitly modeled since they are highly problem-dependent. Small-scale structures, on the other hand, are isotropic and general, making them ideal candidates for simplified modeling. The LES is currently among the models with the highest level of accuracy, but they are not further studied as they have a computation complexity since they are heavy compared to the processing power of the computer utilized in the study.

Most of those computational codes published to date are based on RANS models, which were the first to be developed. They are generated by applying the so-called Reynolds decomposition to the classical Navier-Stokes equations (i.e. the rewriting of each flow variable φ as the sum of the average contribution $\overline{\varphi}$, averaged over time and on oscillating φ' which is depending on time instant.

The essential benefit of the previously mentioned models over LES models is their lower computational complexity, which makes them desirable in both industry and academic environments. We can indeed distinguish two macro-categories among RANS models, namely one and two-equation models. However, only those corresponding to the second type will be described in this section because they are less dependent on empirical assumptions and hence more generic and suited for the simulations carried out in the following chapter.

The model k- ε and the model k- ω are two RANS equations models that are mentioned. In both cases, the first equation consists of the turbulent kinetic energy transport equation k, written so the dissipation rate ε appears in the first case and the turbulence characteristic frequency ω in the second case.

Throughout the case of the first equation, the first term introduces the transport of ε characterizes the temporal or spatial scale of turbulent fluctuations, while in the second equation the symbol k indicates the intensity of turbulent fluctuations. The two equations that define the phenomenon can be written as follow:

$$\frac{\partial \rho \varepsilon}{\partial t} + \frac{\partial \rho (u_i) \varepsilon}{\partial x_i} = \frac{\partial}{\partial x_j} \left[\left(\mu + \frac{\mu_t}{\sigma \varepsilon} \right) \frac{\partial \varepsilon}{\partial x_j} \right] + C_1 \frac{\varepsilon}{k} \mu_t \left(\frac{\partial u_j}{\partial x_i} + \frac{\partial u_i}{\partial x_j} \right) \frac{\partial u_j}{\partial x_i} - C_2 \frac{\varepsilon^2}{k} \rho \quad (4.19)$$

$$\frac{\partial \rho k}{\partial t} + \frac{\partial \rho (u_i) k}{\partial x_i} = \frac{\partial}{\partial x_j} \left[\left(\mu + \frac{\mu_t}{\sigma k} \right) \frac{\partial k}{\partial x_j} \right] + \mu_t \left(\frac{\partial u_j}{\partial x_i} + \frac{\partial u_i}{\partial x_j} \right) \frac{\partial u_j}{\partial x_i} - \rho \varepsilon \quad (4.20)$$

The Prandtl – Kolmogorov relation is used to calculate the turbulent viscosity μ_t and it can be written as follow:

$$\mu_t = \rho C_\mu \frac{\varepsilon^2}{k} \quad (4.21)$$

Where C_1 , C_2 , C_μ and ρ_k are the numbers of Prandtl turbulent per k, whereas ε_ρ is the number of Prandtl turbulent per ε , and they are constant.

The drawback is that such equations are not applicable to the viscous/conductive substrate found on the wall areas. In general, introducing the term wall functions is meant to insert the fluid boundary conditions to link the temperature and the velocity of the computation node close to the wall.

$$\frac{\partial \rho \omega}{\partial t} + \frac{\partial \rho (u_j) \omega}{\partial x_j} = \frac{\partial}{\partial x_j} \left[\left(\mu + \frac{\mu_t}{\sigma \omega} \right) \frac{\partial \omega}{\partial x_j} \right] + \frac{5}{9} \frac{\omega}{k} \mu_t \left(\frac{\partial u_j}{\partial x_i} + \frac{\partial u_i}{\partial x_j} \right) \frac{\partial u_j}{\partial x_i} - \beta \rho \omega^2 \quad (4.22)$$

$$\frac{\partial \rho k}{\partial t} + \frac{\partial \rho (u_j) k}{\partial x_j} = \frac{\partial}{\partial x_j} \left[\left(\mu + \frac{\mu_t}{\sigma k} \right) \frac{\partial k}{\partial x_j} \right] + \mu_t \left(\frac{\partial u_j}{\partial x_i} + \frac{\partial u_i}{\partial x_j} \right) \frac{\partial u_j}{\partial x_i} - \beta' \rho k \omega \quad (4.23)$$

The model $k-\omega$, the first equation adopts the use of the transport equation of the turbulence characteristic frequency ω , which in turn can be expected to be proportional to the inverse of turbulent characteristic duration, and it is considered as the time passed between their creation and dissipation.[8]

Referring to the equations (4.10) and (4.11) we can rewrite the Prandtl-Kolmogorov relation as:

$$\mu_t = \rho \frac{k^2}{\omega} \quad (4.24)$$

Whereas, β' , $\beta = C_\mu, \rho \varepsilon = \rho k$ are constant values and they can be found in the literature.

This form of the model has the advantage of being valid in the wall region, which can then be solved and treated such as the rest of the domain. On the other hand, The consequence is that it's extremely sensitive to the amount of turbulence in the free stream, resulting in an overestimation of k in stagnation regions. Moreover, both models have been changed and refined throughout time to improve the accuracy of the results.

Two distinct evolution were considered for this research: feasible $K-\varepsilon$ and SST (Shear Stress Transport). The first approach obtained from $K-\varepsilon$ introducing two changes, the first is turbulent viscosity adopts a new formulation by C_μ which is being changeable rather than constant. A new dissipation rate transfer equation ε derived by mean square vorticity fluctuations would be the second difference.

Overall, the realizable $K-\varepsilon$ model is convenient to flow with significant curvatures, such as those found in the receiver U-tubes. The Shear Stress Transport (SST), linearly combines the classical $K-\varepsilon$ and $K-\omega$ by adopting the first in the free stream and the latter in the wall region. The ratios of the two models are determined by the coefficients F1 and (1-F1), where F1 is the blending function. Meanwhile, in the free current, value 1 is assumed near the wall, and value 0 is in the free current.

Both models offer a decent combination of accuracy and computational time, therefore both were interesting for the case study. The momentum field results were nearly comparable, although the achievable $K-\omega$ required less computational time than (SST). As a result, the reference turbulence model for this investigation was selected. There are only four boundary conditions to consider:

- The boundary condition imposed on the intake section is attributed to the unit area of the pipe section where the airflow is moving.

$$\frac{\dot{m}_{tube}}{A_{tube}} = \frac{\frac{\dot{m}_{tot}}{n_{tube}}}{\frac{\pi D_{tube}^2}{4}} = \frac{\frac{0.1}{12}}{\frac{\pi(0.018^2)}{4}} = 33 \left[\frac{kg}{m^2} \right] \quad (4.25)$$

- A pressure of 2.98 bar is applied to the outlet portion, resulting in a fluid inlet pressure of around 3 bar.
- No-slip condition is established at the pipe walls, $u = 0$.
- Along the symmetry surface of the pipe section included in the domain under analysis imposes the condition of symmetry of the flow, $-u \cdot n = 0$.

Chapter 5

Simulation and model result

5.1 Mesh Independence

The degree of refinement of the calculation domain would be the first thing to be focused on, in any form of computational study (mesh). The higher the density of nodes in the mesh, the more equations to be solved, hence the longer the time to get a solution. As a result, it's a trade-off between accuracy and productivity. Both of these variables are essential because the first depends on the conclusion validity, while the second is a function of the research expenses.

To do so, we assumed a study which was conducted in steady-state conditions with the focused radiative flux of $500 \frac{kw}{m^2}$, or the concentrated flux achievable under $1000 \frac{W}{m^2}$ solar irradiance. Then we changed the number of nodes, gathering five specific parameters for each scenario, which were then the topic of the following research:

- Air outlet temperature T_{outlet} , whose value permits the useful effect of solar heating to be quantified.
- The average temperature of the PCM ($T_{PCM,ave}$), indicates the mitigating effect of the phase change process, which occurs when the material's melting temperature is attained.
- Average liquid fraction, which emphasizes the PCM material's usage quality. It illustrates the volume fraction of PCM in the liquid state in more detail.

- Average liquid fraction χ_l , which emphasizes the PCM material's usage quality. It illustrates the volume fraction of PCM in the liquid state in more detail.

Along with the component the following formula is used to compute the point liquid fraction χ_l :

$$X_{l,i} = \begin{cases} 0, & \text{if } T \leq T_m - dT \\ \frac{T - (T_m - dT)}{dT}, & \text{if } T_m - dT < T < T_m + dT \\ 1, & \text{if } T \geq T_m + dT \end{cases} \quad (5.1)$$

- T_{max} , an important thermal limit parameter for the confinement material (1600 °C), is the highest temperature achieved on the receiving surface.
- $T_{hotwall}$ the average temperature of the hot wall surface (in literature, we refer to the hot wall as the receiving surface), which indicates the significance of radiation losses.

Table 5.1: Types of mesh grid independence computed

Number of cells	T_{wall} °C	T_{out} °C	T_{max} °C	T_{PCM} °C	χ_l %
36995	1155.7	894.8	1249.7	1032.2	94
45870	1146.6	880.3	1255.9	1119.7	84
67039	1143.8	879.8	1253.5	1017.5	82
114131	1143	879.9	1248.9	1016.7	82
198260	1142.3	880	1253.8	1016.5	81

Specific types of mesh were considered and evaluated for the sake of what has been mentioned in the previous paragraph with the results shown in Table 5.1. these results have not exceeded 200,000 elements, otherwise, it takes a longer time to be computed. Yet imposing stagnant conditions required many hours to simulate. These results are offset by a computation time of around one hour, which is considered a reasonable compromise gave the values obtained.

Analyzing the aforementioned data as a function of the relative error, we can see that cell 67039 with relative errors of the four temperatures, all less than or equal to 0.22%, and relative liquid fraction error about 0.76% percent. However, these results are compensated by a computation time of about one hour, which is considered a good compromise with the values obtained.

In terms of meshing, domain discretization was achieved using a predefined COMSOL algorithm that generates a mesh with the necessary element types for the numerical methods chosen. In this particular case, tetrahedral elements of various sizes were constructed within the solid domains while a combination of tetrahedral mesh and boundary layer elements were used within the fluid domain.

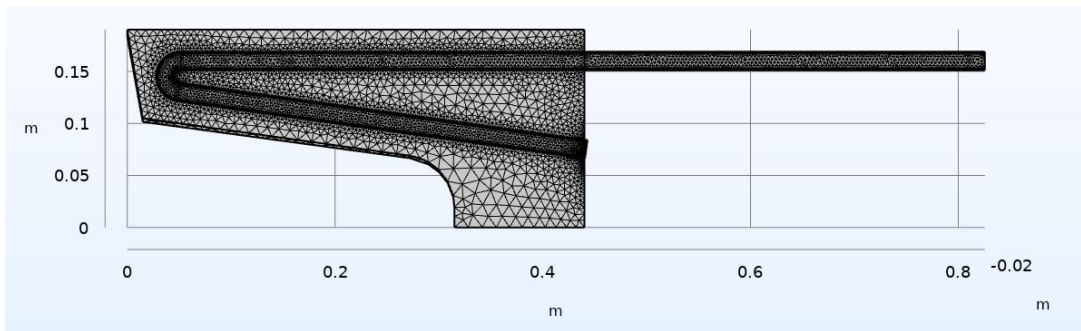


Figure 5.1: Finer mesh

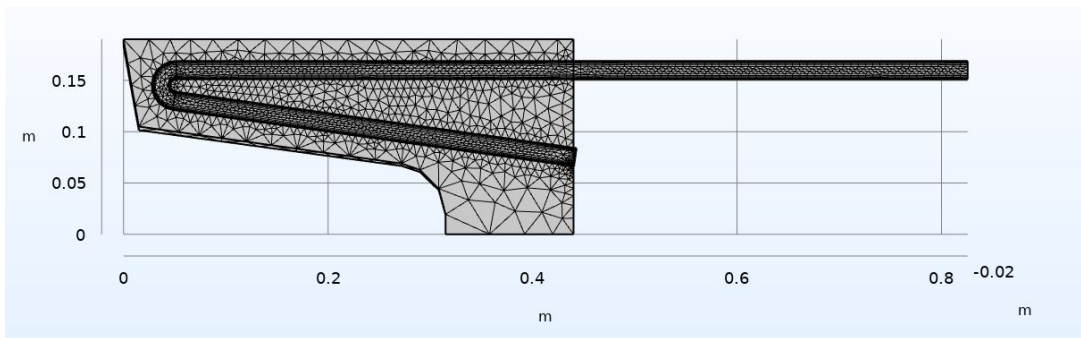


Figure 5.2: Selected mesh

The mesh size was continually adjusted until the conjugate heat transfer became mesh independent in order to obtain precise results. The mesh size was continually adjusted until the conjugate heat transfer became mesh independent in order to obtain precise results. The meshing size of the cross section steadily increased from coarse mesh (1934841 million cells) to fine mesh (2001484 million cells). And liquid fraction became stable after that, it has also been taken into account for the final mesh resolution.

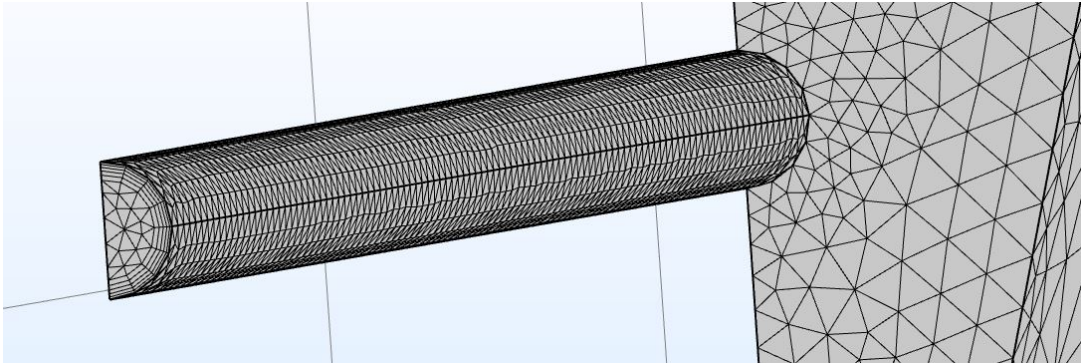


Figure 5.3: Zoom in zone of the air passage tube

The number of boundary elements in the coarse mesh is equal to 4187 , while the fine mesh for is about 4674. Furthermore, number of boundary elements in the coarse mesh is 82829, whereas it increased in case of fine mesh at 90899. The time consuming to build the mesh is also has to be taken into account where it was about 32.80 second for coarse mesh and 33.28 second in case of fine mesh, respectively.

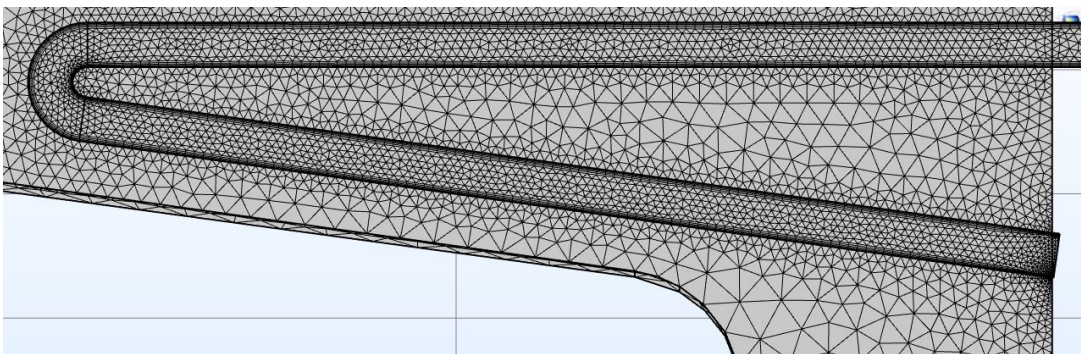


Figure 5.4: Zoom in zone of the air passage tube

The temperature distribution in the PCM follows the predictions in general. The coldest zone is the one nearest to the air inlet portion, while the peaks are mostly found around the bottom of the cavity and the solar ring, around which the PCM begins to heat up and liquefy once exposed to the thermal flux. The presence of the confining material, which is very conductive, allows for the reduction of temperature gradients and better homogenization, has a significant impact on this temperature distribution.

5.2 Analytical formulation of the apparent specific heat

To simulate the phase change, we adopted one of the most popular and widely used approaches for fixed grid models. the method of apparent specific heat means examining an imaginary temperature range involving the phase change temperature and for which the specific heat exponentially increases, in order to account for the latent heat for the material. There are various options to implement this approach, including smoothing the characteristics by constructing the specific heat as a function of stroke and as a Gaussian function, two techniques were investigated in this study; both methods can be shown.

$$X_{l,i} = \begin{cases} Cp_l & \text{if } T < T_f - \frac{dT}{2} \\ \frac{Cp_s + Cp_l}{2} + \frac{dT}{2} & \text{if } T_f - \frac{dT}{2} \leq T \leq T_f + \frac{dT}{2} \\ Cp_s & \text{if } T > T_f + \frac{dT}{2} \end{cases} \quad (5.2)$$

Where in this case $Cp_s = Cp_l + dT$ is the interval temperature in which the phase change occurs.

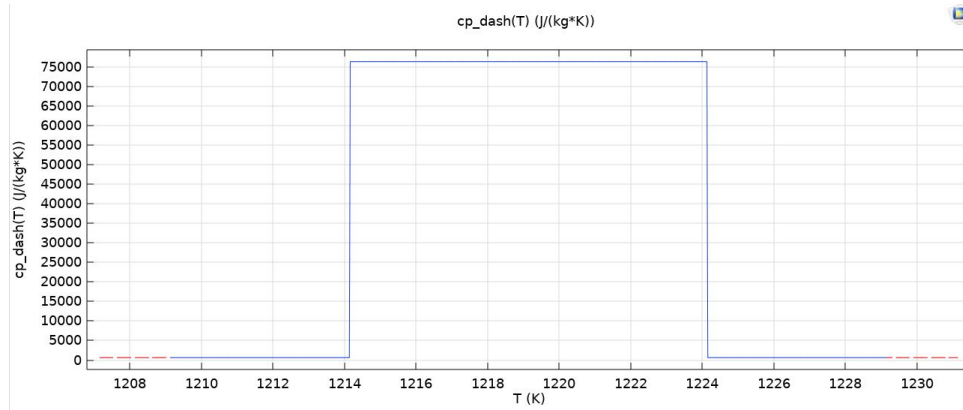


Figure 5.5: Variation of dashed specific heat with temperature

Instead, the Gaussian function is developed so that the areas where one of the two functions is greater than the other are equal to make a comparison. The evident criterion of equality of the subtended areas is also imposed. As a result, Gaussian with a maximum value that is the same as the maximum value of the function at intervals, the analytical expression is as follows:

$$Cp(T) = Cp_s + \frac{L}{dT} \exp(-\sqrt{\pi}) \left(\frac{T - T_f}{dT} \right)^2 \quad (5.3)$$

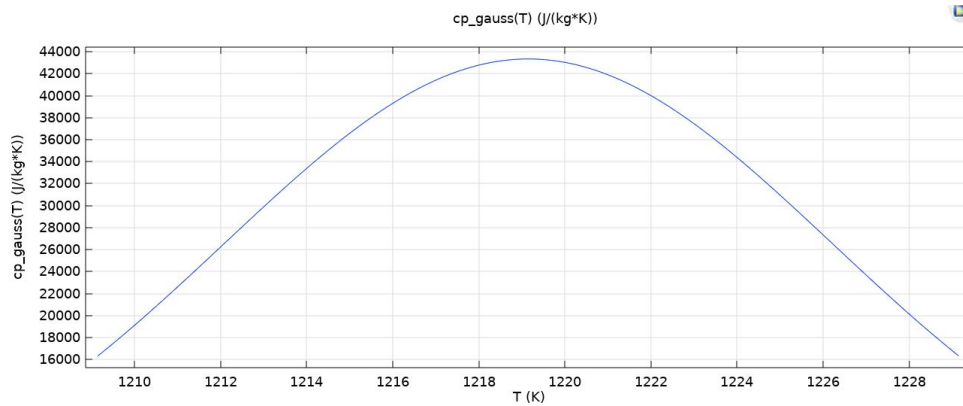


Figure 5.6: Variation of Gaussian specific heat with temperature

However, in order to figure out which method was better, two identical simulations were performed, differing only in the analytical definition of the specific heat. The results of these simulations are in the following table.

Table 5.2: Results of the Simulation in both cases of the Apparent specific heat

Mthod	T_{max}	T_{out}	T_{PCM}	$T_{hotwall}$	χ_l	$u_{average}$	Computing time
	°C	°C	°C	°C	%	$\frac{m}{s}$	[min]
Cp'	1270	804.04	1019.3	947	82.6	25.605	24
Cp,gaussian	1270	804.04	1019.3	947	82.6	25.605	33

In both situations, relative errors show remarkably similar temperature distributions, but with a significant reduction in computing time due to the usage of the Cp', rather than in case of the Gaussian case. As a result, the latter Cp' was considered for the simulation.

5.3 Daily Transient

We proceeded with the study by studying the thermal behavior of the component throughout its operation after the model is created, calculation methods were defined, and a sufficiently precise mesh was chosen. However, The solar radiation inputs used and the initial condition chosen for the transients are described in the following paragraphs, followed by a study of the trends of some specific average parameters during typical days of some months of the year. In addition, two specific cases were examined to highlight the benefits of using PCM and to demonstrate the adaptability of the receiver in conditions defined by high levels of solar radiation intensity.

5.4 Solution Inputs

Data on the irradiance levels obtained during a day in a certain place around the world are required to replicate the operation during a typical day. Since this study was carried out in collaboration with the Energy Center of Turin, solar radiation data measured with a solarimeter were placed on the roof of the research center.

These data, which were measured and gathered every 15 minutes, were analytically handled to produce a continuous analytical function with the time needed to approximate these data.

The type of function selected is a Gaussian function with the following form:

$$G = \begin{cases} A \cdot \exp\left(\frac{(t-t_0)^2}{C}\right) - D & \text{if } A \cdot \exp\left(\frac{(t-t_0)^2}{C}\right) - D > 0 \\ 0 & \text{if } A \cdot \exp\left(\frac{(t-t_0)^2}{C}\right) - D \leq 0 \end{cases} \quad (5.4)$$

A, C and D are constants different in each month optimized utilizing the Excel "solver" tool and calculated using the experimental data and the analytical curve, and maintaining an area subtended by the analytical curve at least equal to that subtended by the experimental results.

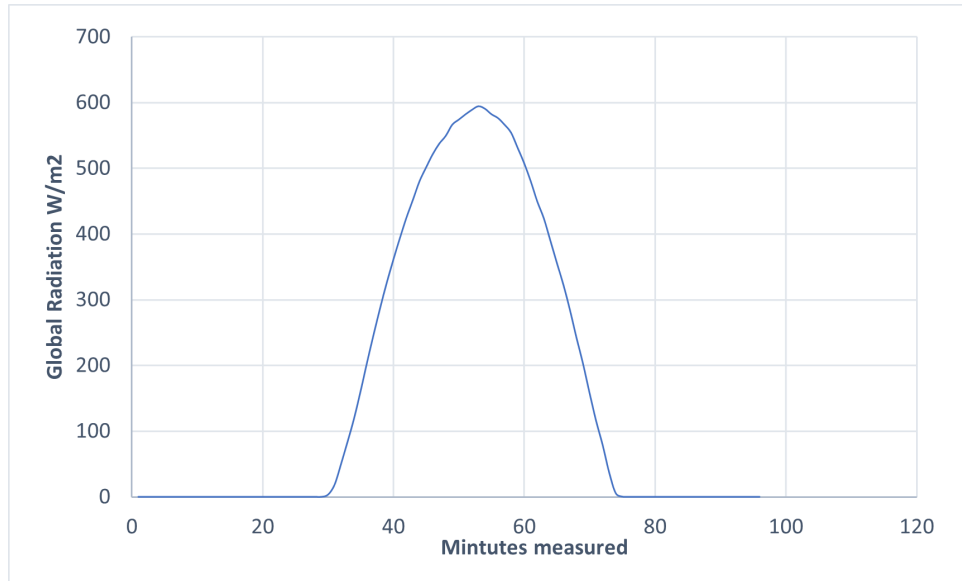


Figure 5.7: Energy Center data collected Represent the Radiation values changing with time

5.5 Initial conditions

The exact definition of the initial temperature distribution is a rather complex problem. There are two difficulties in particular: the first is that some of the assumptions of the model are valid only in the period of operation of the system for which the irradiance values are high and the sun is high; the second is that we do not have much information about the transition between conditions and which for example the airflow rates could be different.

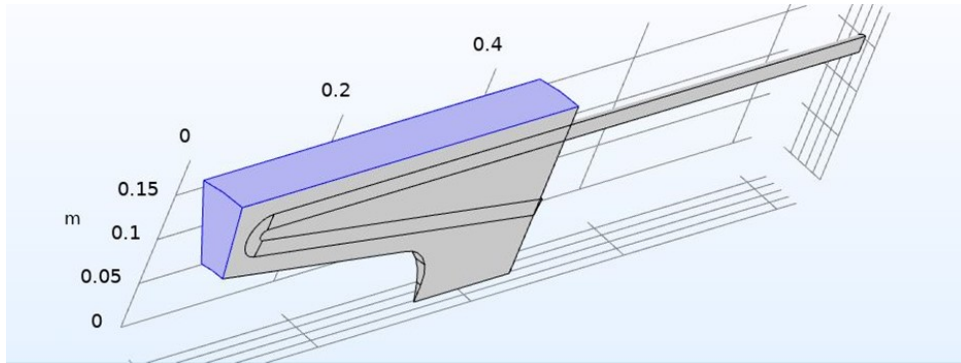


Figure 5.8: Lateral and upper cross section view

As a starting point, the temperature distribution obtained from the study under stationary receiver conditions with an induced heat flux equal to the minimum required to create airflow with a temperature of 800°C at the receiver outlet was chosen. The theory is conservative because with the system turned off, the lack of a fluid running through the tubes allows for rapid heating of the component, resulting in temperatures higher than those previously assumed.

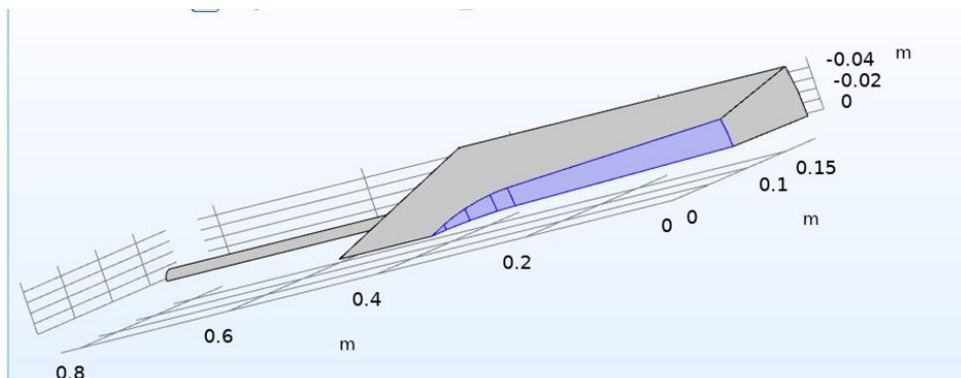


Figure 5.9: Inner view of the model geometry

As we can see from Figures 5.8 and 5.9 we included the outer and inner surfaces of the confinement material to see the inward radiation flux. The approach we followed in our calculation is that the outer and the upper surfaces of our geometry were examined. Also the convection losses corresponding to the radiation are important to be taken into account and they have been calculated as follow:

$$\text{Inward Heat Flux} = \text{Absorption} * irr * \pi * \frac{r_1^2 - r_2^2}{s_1} * [24 - h * (T_i - T_{ambient})] \quad (5.5)$$

$$\text{Inward Heat Flux} = 24 * irr * \pi * \left[\frac{r_2^2 - r_3^2}{s_2} + \frac{r_3^2 - r_4^2}{s_3} + \frac{r_4^2 - r_5^2}{s_4} + \frac{r_5^2 - r_6^2}{s_5} + \frac{r_2^2 - r_3^2}{s_2} + 0.9 \right] \quad (5.6)$$

Where, r_1, r_2, r_3, r_4, r_5 and s_1, s_2, s_3, s_4, s_5 are the radius and thickness of each part of the cavity geometry. As shown in figure 5.9

Whereas, we split the inner ring into one large area and the rest were 4 small areas. Considering irradiance equal to 500 kW/m^2 we got inward heat flux equal to 448.13 kW/m^2 from the upper and the outer surface and the inner ring surfaces is about 979.85 kW/m^2 . And this result is quite high because the inner geometry is influenced by the fluid temperature which is flowing inside the tube at high temperature.

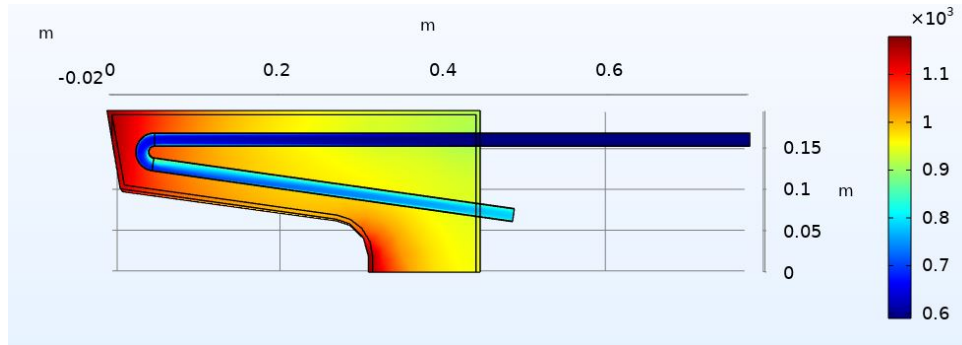


Figure 5.10: Temperature distribution for the mesh selected

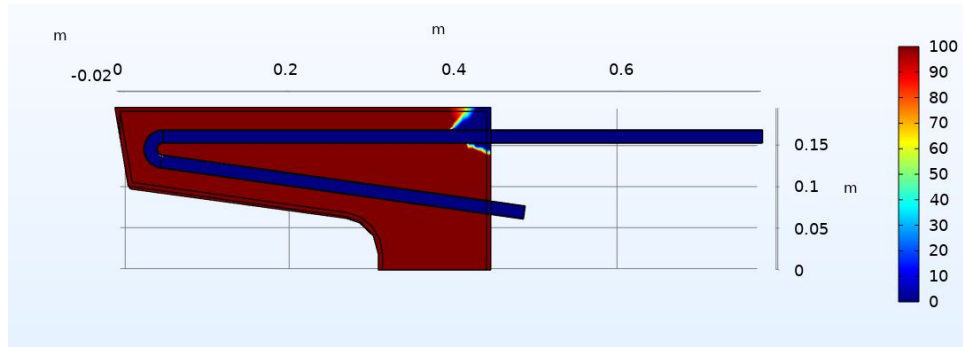


Figure 5.11: Liquid fraction contour for the mesh selected

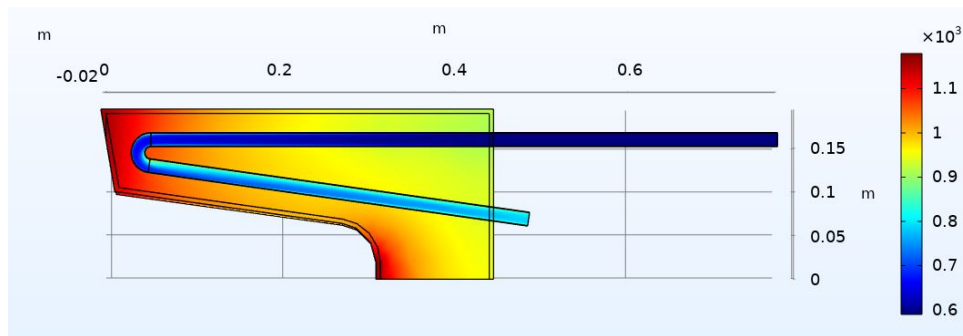


Figure 5.12: Temperature distribution in case of more accurate mesh

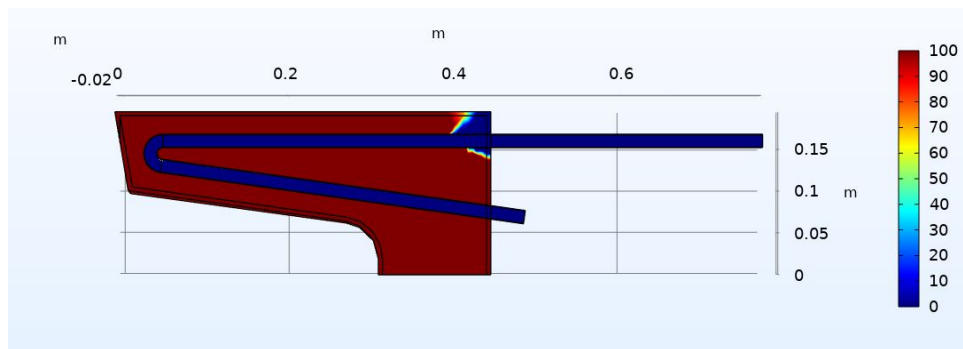


Figure 5.13: Liquid fraction distribution in case of more accurate mesh

The temperature variation that occurs inside the component during the day, in theory, causes a change in the air density, which influences its field of motion. A significant change in the field of motion can result in a change in the quantity of heat dissipated, therefore it's crucial to consider what has just been mentioned. Temperature profiles and PCM liquid fractions are shown for the time-step is set for 9 hours with step size of 60 seconds.

The stationary study was implemented with an applied heat flux of $500 \text{ kW}/\text{m}^2$ and the motion field acquired from the stationary study defined the transient onset condition to validate the importance of this variation.

Table 5.3: Results of the Simulation in both cases of the Apparent specific heat

Hypothesis	T_{max}	T_{out}	T_{PCM}	$T_{hotwall}$	χ_t
	°C	°C	°C	°C	%
Change in velocity	1270	804.04	1019.3	947	82.6
Initial conditions (Stationary)	1270.3	804.08	1019.7	947.8	82.6
Relative Error	0.03%	0.04%	0.04%	0.08%	12%

As a result, the hypothesis of maintaining the fluid velocity field constant does not result in significant errors. Nevertheless, all the reference temperatures derived following this hypothesis illustrate extremely small relative errors as we can see less than or equal to 0.08%. This is a great outcome because the most expensive calculation is in the case of turbulent fluid flow.

As a result, using a constant velocity field during the transient permits the calculation time to be reduced. Because a simulation produced by recalculating the flow field for each time step has never been fully finished. An estimate of the reduction in computation time is not supplied in this example. This is the reason why there are just a few temperatures that could be determined after around an hour, which implies exaggerated calculation time for the entire transient.

5.6 The months of summer and spring

A time dependence analysis was carried out for the selection of an acceptable time step, starting from the initial condition described in the previous section, which assumed a constant turbulent flow field approximation. imposing transient conditions varies depending on the month in which we have been taken the study, noticing that the investigation started from March to August and approximately 9 hours which are roughly the average duration evaluated in this study.

In this discussion, we studied the variation of the phase change material as well as the outlet air temperatures among the period which has been mentioned in the previous graph. We considered that we would have direct normal radiation of approximately 500 kW/m^2 . We also took into account the liquid fraction and the change in the maximum temperature can be obtained in the study.

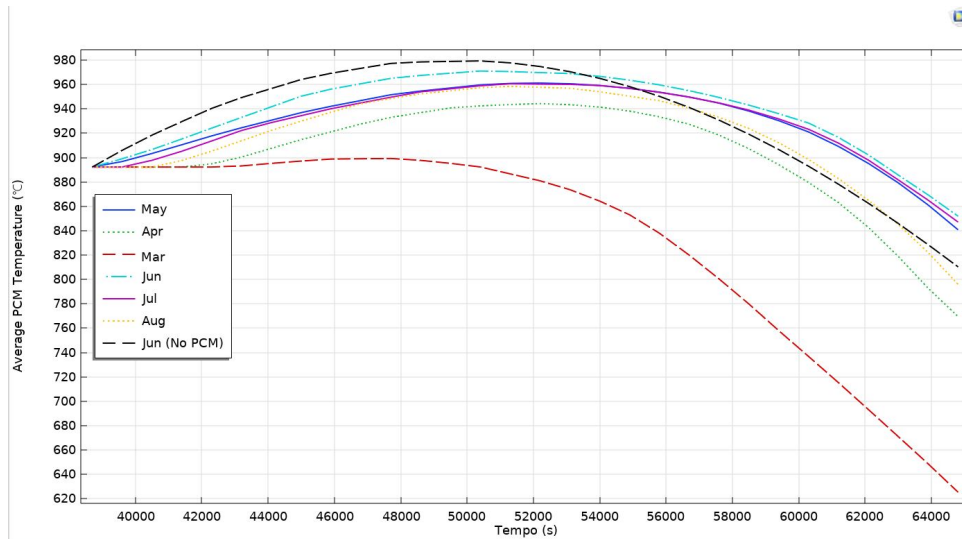


Figure 5.14: Average temperature of the PCM during the period of operation in the various months of the year

In the thermal energy storage systems, the selection of desirable PCM is a challenging task. In fact, the decision of choosing a convenient PCM requires a careful investigation. The months studied in the simulations are those between March and August, as they are the ones for which we can identify irradiance values high enough to allow for the acquisition of an output temperatures capable of ensuring the proper functioning of the micro turbo-gas.

Assuming that May the maximum temperature varies between $19 \text{ }^\circ\text{C}$ to $22 \text{ }^\circ\text{C}$. the Consequently, the entire treatment is set up with a time step of about 7 hours, and considering the maximum radiation we may get at $22 \text{ }^\circ\text{C}$, and at 500 kW/m^2 , we obtained the above-mentioned chart. Noticing that we evaluated the variation of the temperature during the month of June since we may get the highest maximum temperature we may have as the range is between $23 \text{ }^\circ\text{C}$ to $28 \text{ }^\circ\text{C}$.

Overall, figure 5.14 is showing that the average temperatures during the whole months of the study reached are started from 10 am and continues till 6 pm. The study came up with a maximum PCM temperature of $857 \text{ }^\circ\text{C}$ which was obtained in June at 14:30 pm.

Whereas, it's about 800 °C in March. The proper time range for obtaining the maximum temperature among all the months started from 1 pm to 5 pm. In case of not having PCM in the simulation the trend exhibits a smooth increase from 9 am and reached the maximum at 2 pm at about 860 °C and then the curve is dramatically declining to it's the lowest temperature at 6 pm by 733 °C.

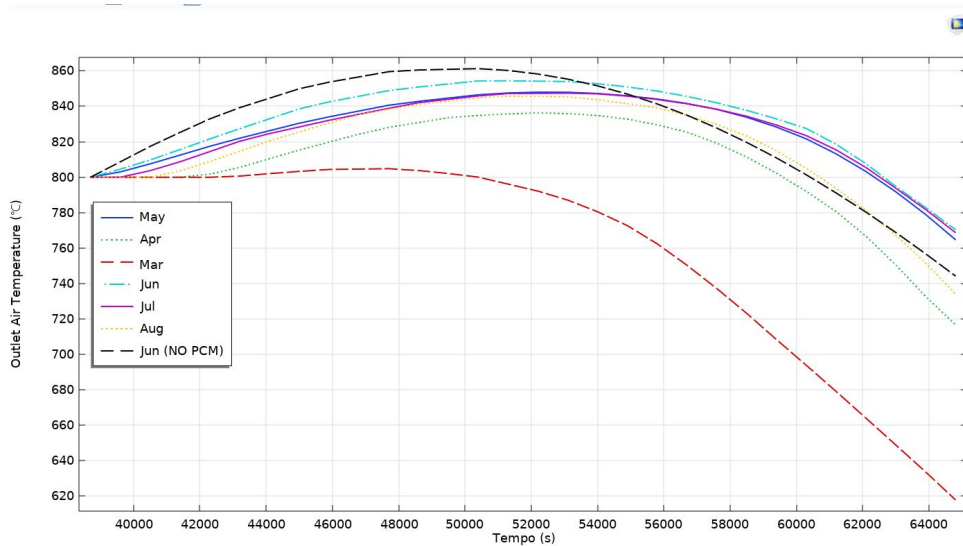


Figure 5.15: Average temperature of the Air outlet during the period of operation in the various months of the year

The solar receiver in the Dish-MGT should feed heat to the working fluid (Air), allowing it to maintain more or less constant outlet temperature. Nonetheless, there are instant variations in the solar radiation impinging on a dish, and even short-term changes can significantly affect the outlet air temperature for receivers with little thermal inertia. The MGT is subject to these changes in terms of performance loss and, in the worst-case scenario, MGT damage. The solar receiver should have sufficient thermal inertia to provide steady system behavior.

As shown in Figure 5.15, illustrates the outlet air temperature change with time during the spring and summer seasons. Overall, the highest temperatures reached by air are between 800°C and 855°C. Among all the months for a period of operation ranging from five to seven hours per day distributed in a period between 10 am and 6 pm, depending clearly on the month considered. The maximum air temperature range (830-850) °C was obtained in June from 12 pm to 4 pm.

In sharp contrast to this, In March we have the lowest range where it started at 9 am by 800 °C followed by a light increase to 805 °C, before being decreased to the lowest value of 615 °C at 6 pm, which reveals that the months of march is considered as the worse period to obtain sufficient values among the whole period of our study.

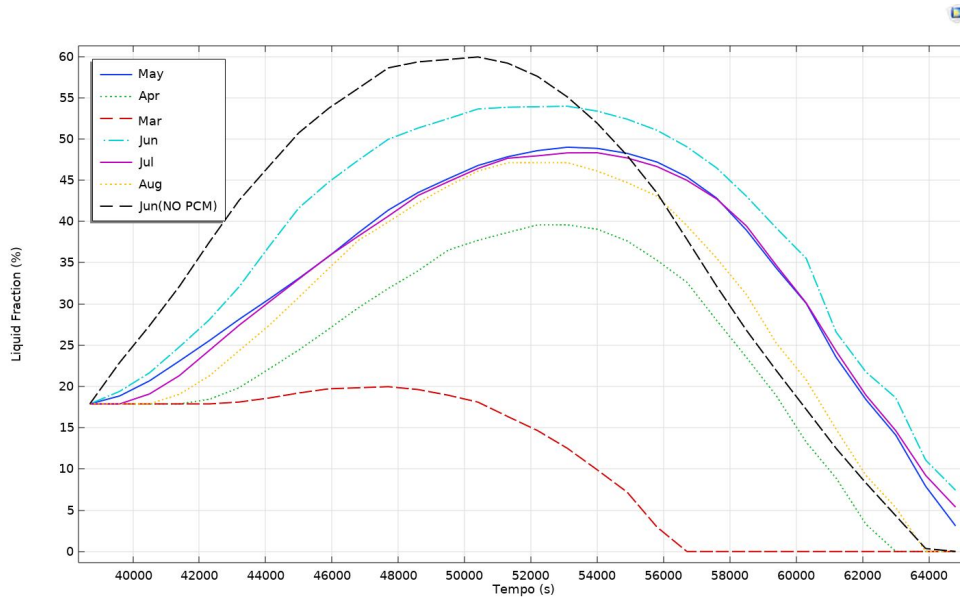


Figure 5.16: Liquid fraction of the PCM during the period of operation in the various months of the year

The PCM is set at ambient temperature (15°C) at the start of the charge phase. The PCM absorbs heat from the cavity wall and begins to melt throughout the charging process. The melting of the PCM increases as it moves away from the heated wall, and the PCM stores latent (and sensible) heat.

The line chart given above compares the liquid fraction χ_l % variation with time during the period chosen in our simulation. The peaks of the liquid fraction are approximately between 18% and 54%, reached respectively from March to August. All trends show a very gradual and almost linear initial growth, then a diminishing slope as the sunsets. Both at the beginning and at the end of the period of operation, the value is around 20%, a limit value below which the system can no longer work.

The trend in the case of March shows a rapid melting of the PCM where it's started to melt after 3 pm over the given period. Conversely, May illustrates the slowest melting value in which the time needed to discharge is roughly 8 hours.

Meanwhile, the melting behavior during June represents a fluctuation between 4 pm and 5 pm, at liquid fractions 36% and 10%, respectively

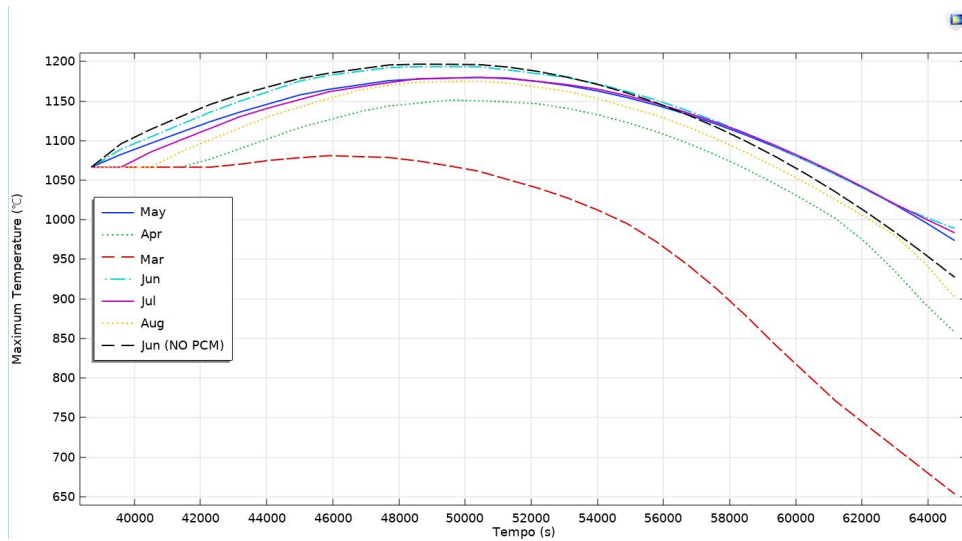


Figure 5.17: Maximum Temperature of the PCM during the period of operation in the various months of the year

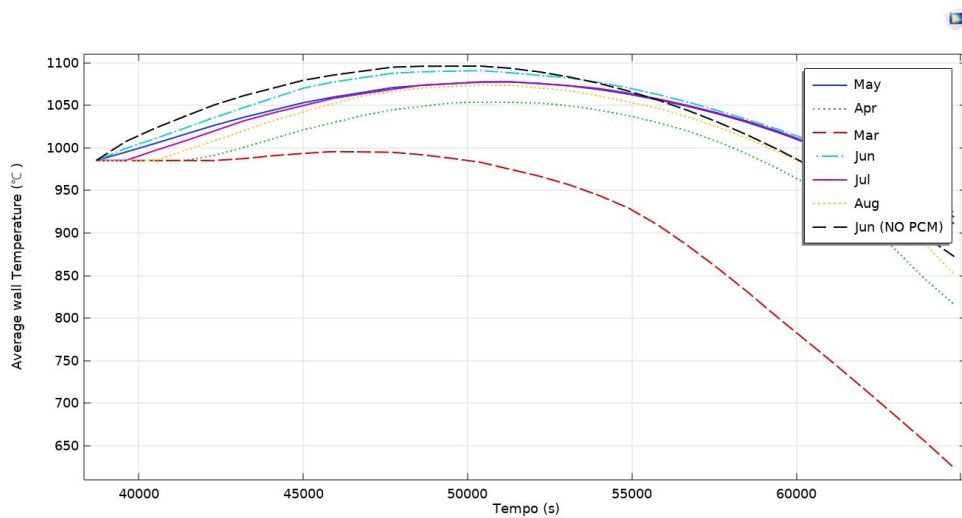


Figure 5.18: Average wall Temperature of the PCM during the period of operation in the various months of the year

The receiver front surface is designed with a conical cavity. As a result, the receiver radiation absorption capacity increases, reducing the hot wall temperature and, Thus, the re-radiation effect. The trends of the average wall temperature and the maximum temperature reached in the component (corresponding to the maximum peak temperature reached on the hot surface of the receiver) show instead trends more similar to that of solar radiation.

Trends are motivated by the fact that the receiving surface is in-direct contact with solar radiation and is therefore not affected by the thermal inertia of the receiver. However, the maximum temperature could be obtained on a mid-day by 1185°C during June, not far from the trends of July and May at roughly 1165 °C. Whilst in March the maximum temperature would be attained between 12 pm to 2 pm with an average of 1060 °C.

Wall temperatures show a percentage variation between 8% and 10% depending on the time of day. The temperature values never exceed 1190°C, thus remaining well below the maximum limit allowed by the chosen PCM for our simulation. The thermal and mechanical performance of the receiver is influenced by the thickness of the walls of the receiver, which causes a barrier to heat transfer. Furthermore, balancing the design of our component is important to ensure the mechanical strength by making the wall thick enough, at the same time thin properly to minimize the heat resistance and thermal stresses.

5.7 Effect of Solar irradiance

The direct irradiance design (DNI) varies from region to region. For CSP design, the reference values of (DNI) chosen were ranging between 500 kW/m^2 to 700 kW/m^2 , those values occurring in clear sky conditions these achievements of irradiance values already quite high. CFD simulations have been performed and revealed that using solar radiation below 500 kW/m^2 is not compatible with the thermal storage capacity of the PCM due to the friction inside the receiver. so we decided to start with the aforementioned values in order to better perform our simulation.

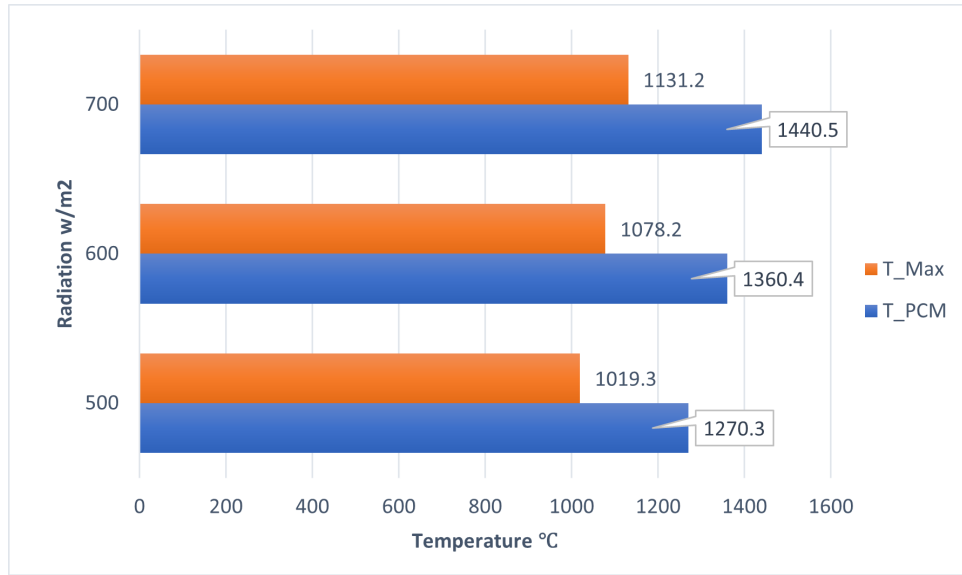


Figure 5.19: Effects of changing the radiation applied on PCM and Maximum Temperature achieved

Solar radiation changes also can arise during the day, depending on cloud motion, it would have a substantial impact on the performance of the system. In the designed receiver the aperture (the frontal area of the receiver) receives the solar radiation coming from the dish concentrator in an area range (56 to 60) m^2 .) [28] with a diameter of the receiver 0.38 m and 0.018 m as a diameter of the inner tubes. In the case of solar radiation applied equally to 500 kW/m^2 , 600 kW/m^2 , and 700 kW/m^2 .

Simulations have been carried out taking into account a day in which there were significant fluctuations in solar radiation. The above figure presented provide the results of different simulations in which we considered the three irradiance value which has been represented in the previous paragraph.

Overall, the most prominent feature is that the value of resulted in T_{PCM} has reached the maximum value at about 1440.5 °C obtained under global solar irradiance equal to 700 kW/m^2 . which is significantly higher compared with the case of 500 kW/m^2 and 600 kW/m^2 where they were 1270.3 °C and 1360.4 °C. The maximum temperature that can be obtained is also taken into account in this calculation whereas we can see from the graph it reached its maximum under a radiation value of 700 kW/m^2 by 1131.2 °C and its lowest value under radiation equal to 500 kW/m^2 by 1019.3 °C.

The time step calculation has been reduced in the following simulations to be able to take into account the discontinuity of radiation function, the following figures presented the results of two different simulations: the blue trend illustrates to the operation of the solar receiver as it has been described so far; the green curves were attained in case of eliminating the physics of Phase change materials from our model. However, the comparison between the two curves should therefore give an idea of the influence which result by using the latent rather than sensitive thermal accumulation in case of equal volume conditions. Hence, it is obvious how to use relatively small quantity of PCM allowing to substantially to reduce the effects given by sudden changes in solar radiation.

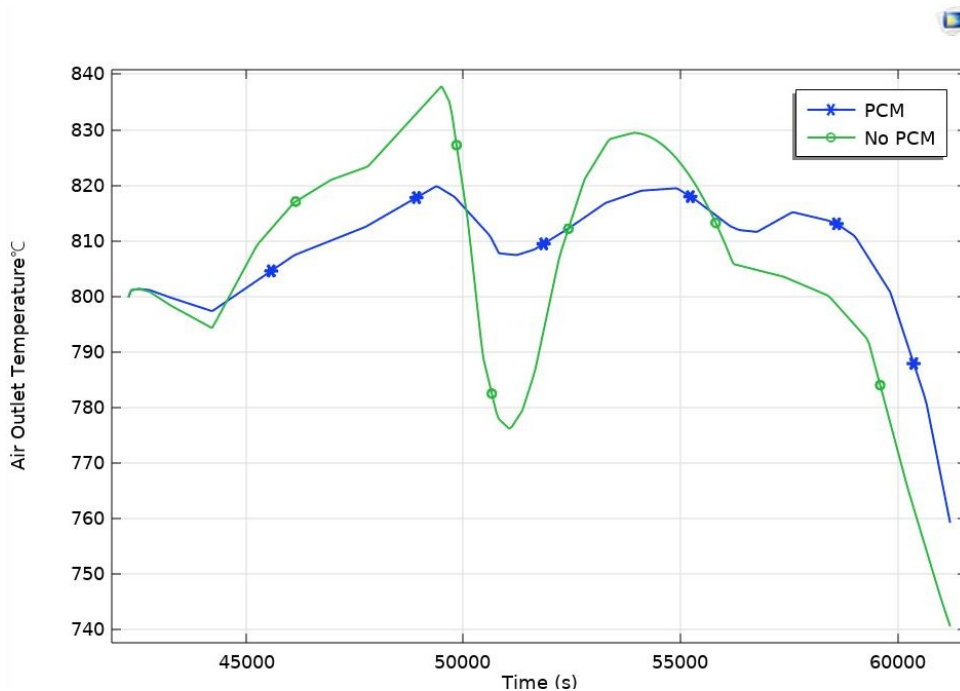


Figure 5.20: Effect of solar radiation fluctuation on the outlet air temperature

In fact, despite the rapid drop in G around 1:45 PM, the temperature at the air outlet (blue curve) in the presence of PCM remained relatively steady during the day, with only minor instantaneous temperature changes. The same cannot be said for the orange curve, which displays an average temperature gradient of 3°C each minute between 13:45 and 14:05, resulting in a total temperature variation of 60°C in just 20 minutes. Figures 5.21, 5.23, and 5.24 all exhibit similar trends, with very minor changes.

As explained in paragraph 5.6 the wall temperature reflects more solar radiations comparing with the other alternative temperatures which have been considered in our simulation.

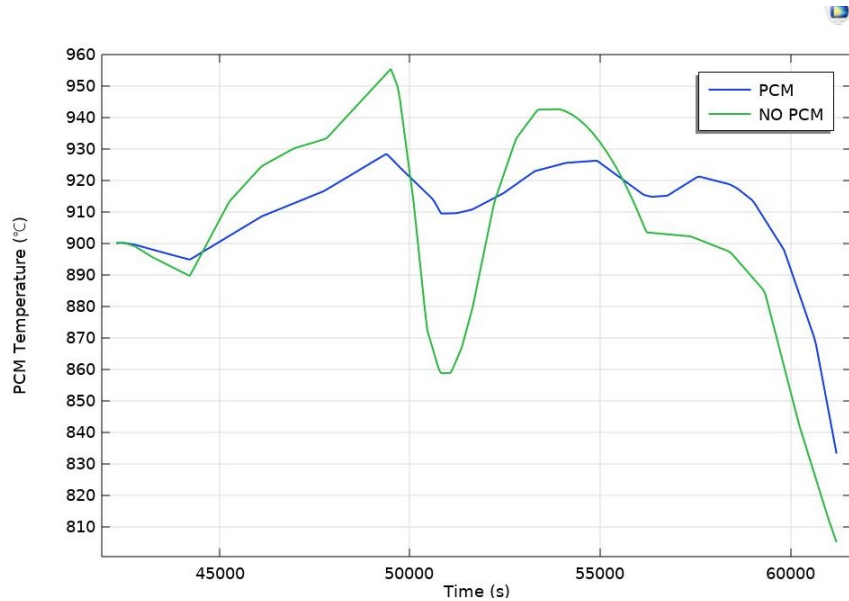


Figure 5.21: Effect of solar radiation fluctuation on the average PCM temperature

Referring to the liquid fraction curve, we can figure out that the temperature differences between the green curves among the graphs which we obtained show that the more they are obvious the larger the liquid fraction in case of PCM presence.

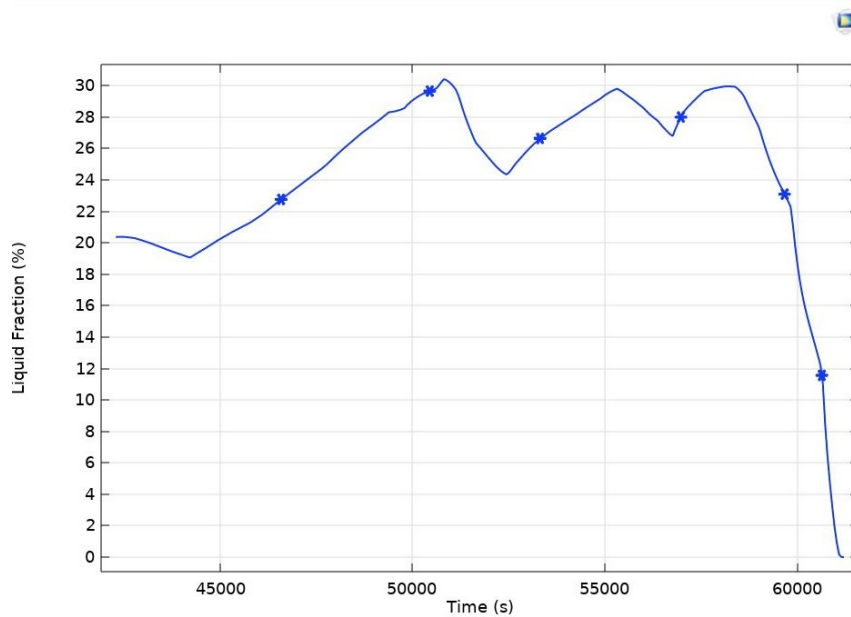


Figure 5.22: Effect of solar radiation fluctuation on the Liquid Fraction

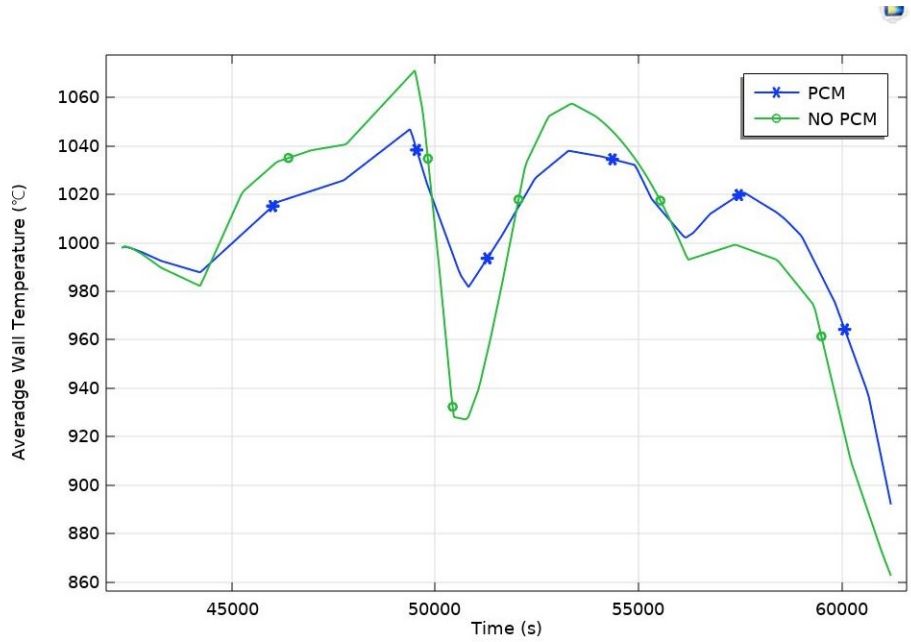


Figure 5.23: Effect of solar radiation fluctuation on the average wall temperature

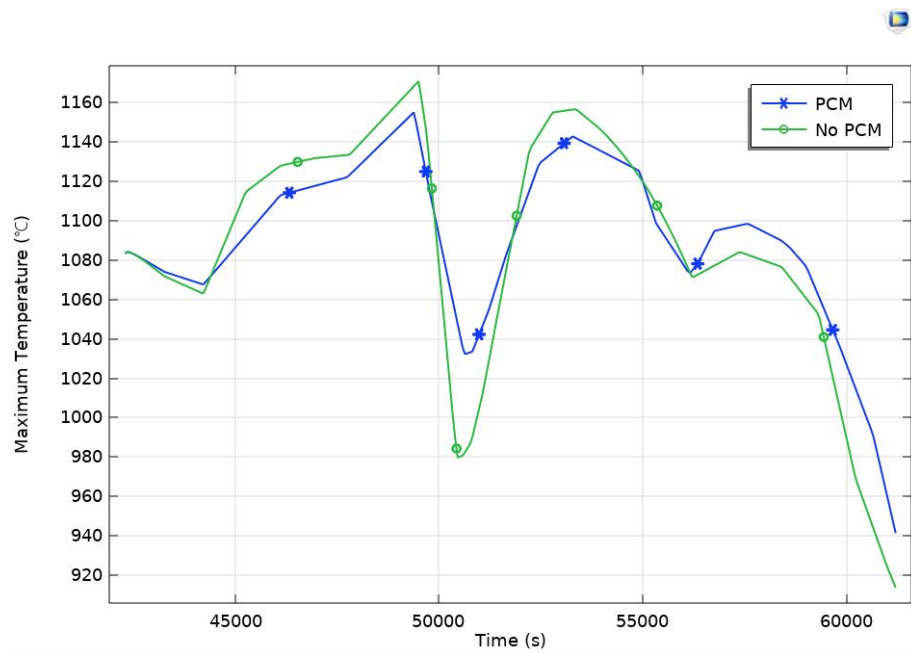


Figure 5.24: Effect of solar radiation fluctuation on the Maximum temperature

Considering the wall temperature obtained in case of fluctuation of the solar radiation, the most significant feature is that during the time from 2 PM and last for about 20 minutes the temperature in case of No PCM included in our geometry decreasing by two folds than in case of PCM, by reaching 930 °C and 990 °C, respectively. Moreover, the fluctuation in the trend of NO PCM seems to be quite rapid compared with the case of PCM usage, implying that in case of having such kind of radiation discontinuity, it is preferable to utilize the PCM in our design to prevent the rapid variation of the temperature.

5.8 Effect of changing PCM

The melting and solidification of PCM in our geometry, as well as its orientations for heat storage in solar thermal systems, are interesting factors. The temperature of the heat transmission fluid and the initial temperature of the storage material are important operating parameters in PCM melting. In the following section we will show the effect of changing the PCM and its effect on the parameters which have been discussed previously.

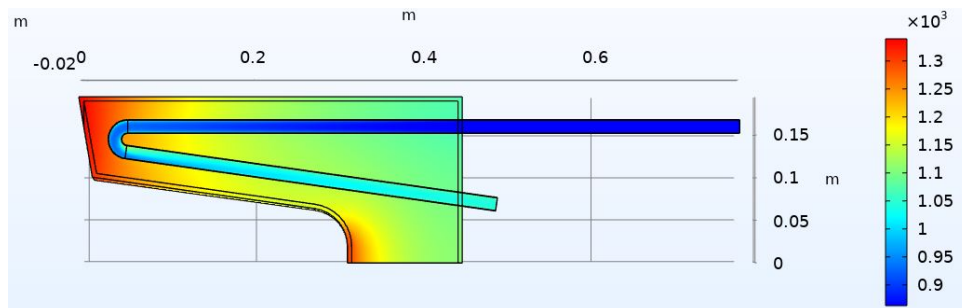


Figure 5.25: Temperature distribution profile for NiSi

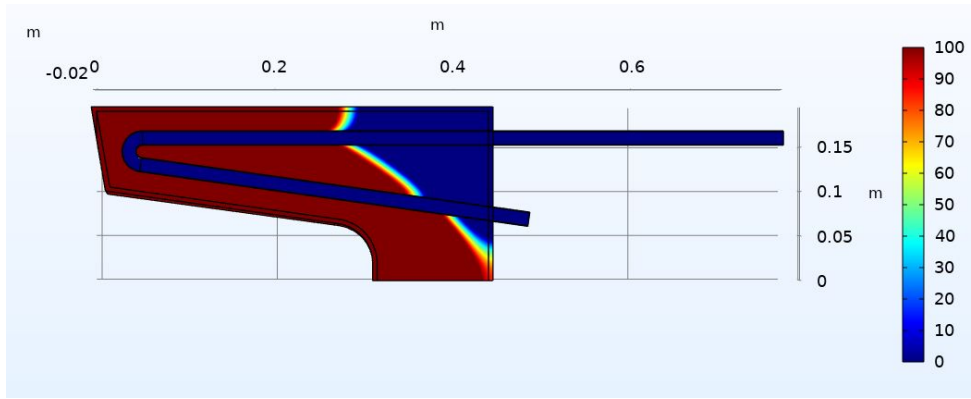


Figure 5.26: Liquid fraction contour for NiSi

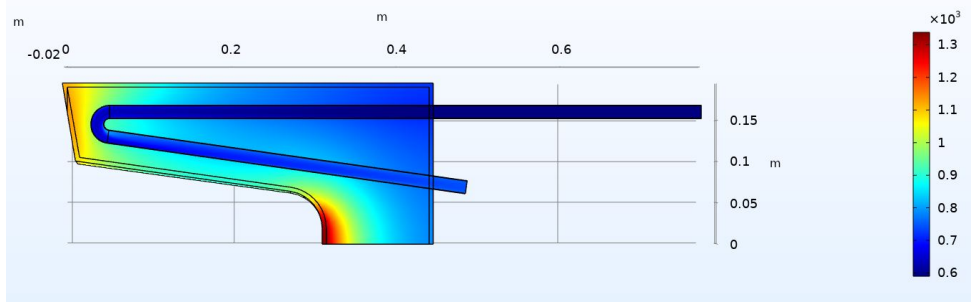


Figure 5.27: Temperature distribution profile for AlSb

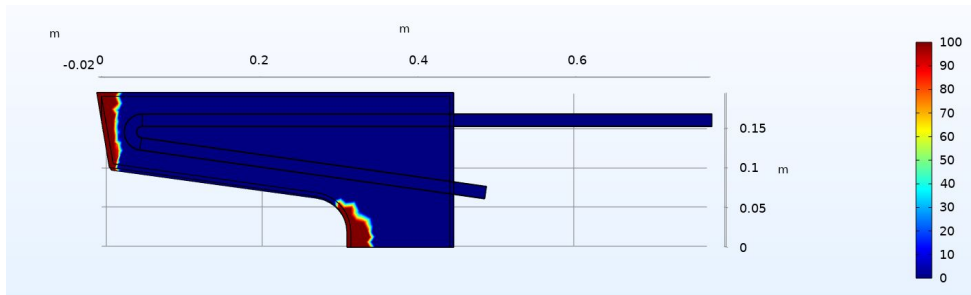


Figure 5.28: Liquid fraction contour for AlSb

The front surface of the receiver is heated by focused solar radiation, which heats the PCM inside the volume. The PCM is heat storage and transfer medium that stores sensible and latent heat while also transferring some of it to the compressed air inside the tubes.

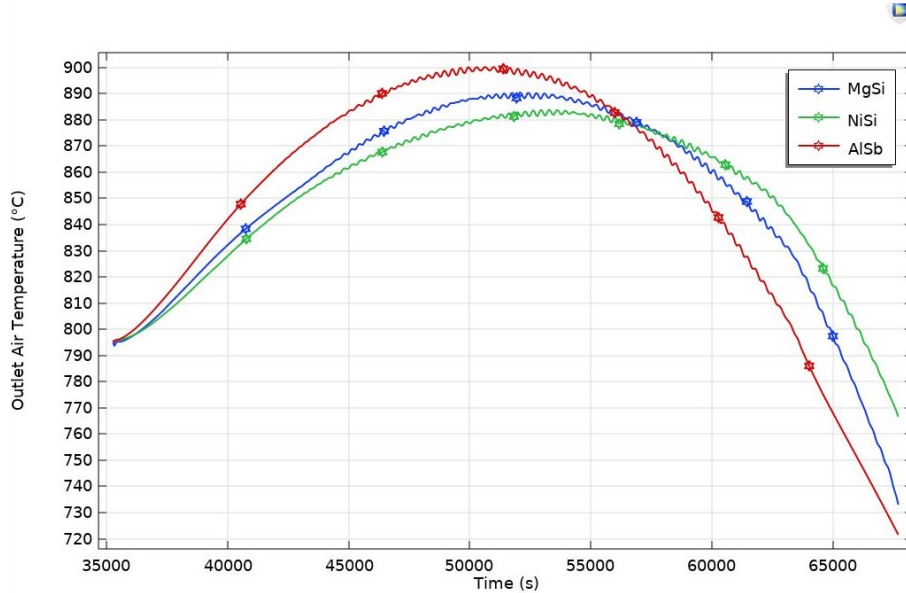


Figure 5.29: Comparison of the outlet air temperature by considering the selected PCMs during the radiation time

In this study, we considered that the maximum value of radiation would be obtained during June. as a result, we built up our simulation based on designing at the maximum values. However, the temperature stability of the air entering the expander is a critical concern. To overcome the natural variations of solar radiations and create a constant behavior of the outlet air temperature, short-term thermal energy has been stored inside the receiver.

The AlSb produces slightly higher outlet temperature by 900.25 °C at 2 PM compared with those in MgSi and NiSi, by 888.90 °C and 881.46 °C, respectively. The outlet air temperature for all PCMs maintain temperatures higher than 850 °C after their complete melting state.

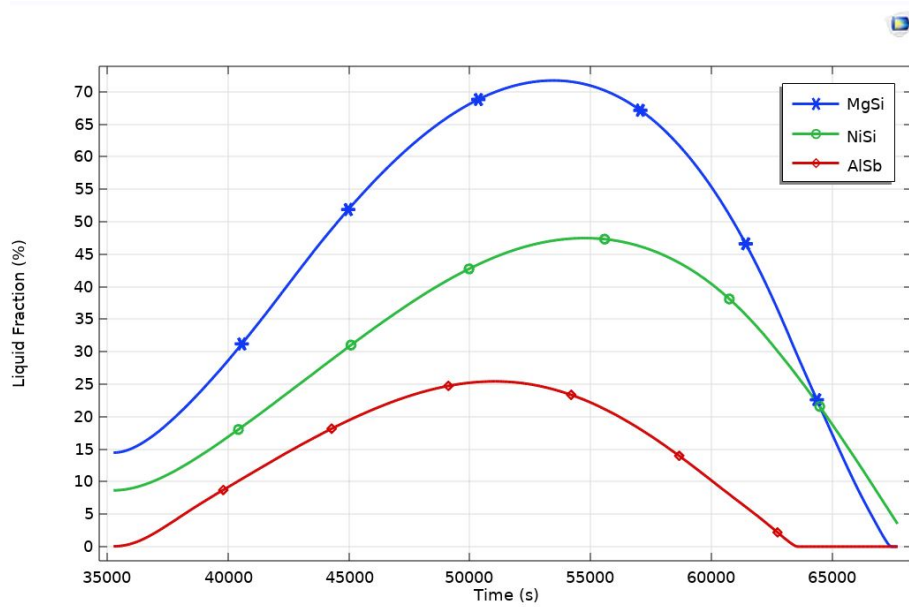


Figure 5.30: Comparison of the Liquid fraction by considering the selected PCMs during the radiation time

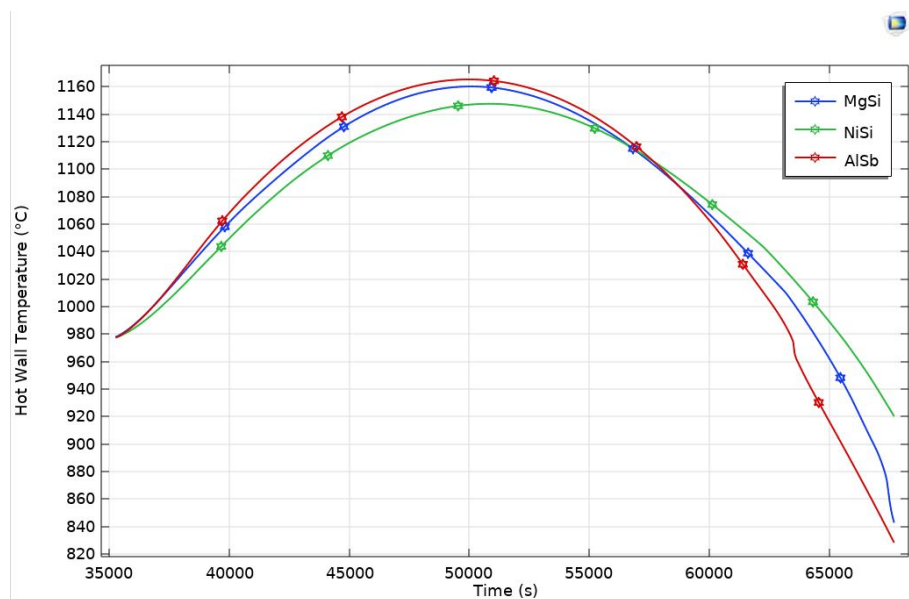


Figure 5.31: Comparison of the wall temperature by considering the selected PCMs during the radiation time

A severe discharge process carried out starting from the standard conditions and transient simulations were performed. The discharge process was evaluated for about 9 hours. After completing the solidification, the charging phase of the PCMs is executed considering the solar flux is directed to the cavity front gate. The results of the solidification phase were satisfactory.

As It can be seen in Fig 5.30 that due to the high melting temperatures for Alsb and NiSi, hence they show low liquid fraction by 22.5% and 47.5% compared with MgSi by 71%. The Alsb has low latent heat of fusion and low specific thermal conductivity, hence quick solidification. MgSi and NiSi show continuous solidification processes. Whereas, they completely solidify after about 9 hours where in case of using Alsb it was roughly 7 hours.

The simulation carried out under the solar radiation of $500 \text{ KW}/\text{m}^2$ and reveals that the maximum wall temperature in all confinement material which have been imposed is $1600 \text{ }^\circ\text{C}$. Consequently, they are all working below the maximum allowable range set by the receiver cavity material. maximum hot wall temperature could be achieved in case of using Alsb at about $1060 \text{ }^\circ\text{C}$ nearby the upper face of the solar receiver, while it reached to $1055 \text{ }^\circ\text{C}$ and $1043.5 \text{ }^\circ\text{C}$ in MgSi and NiSi, respectively.

Conclusion

Taking into account the various simulations and comparisons made, the study investigates an innovative thermal storage technology for plants that use a solar disk concentrator. The objective of this work was to describe the approaches for virtually modeling a micro-turbo gas component. This is done, in particular, to simulate its operation and evaluate the benefits of integrating it into the solar receiver. The goal of this integration is to enhance the thermal behavior of the receiver in order to reduce the impacts of solar radiation fluctuations caused by passing clouds temporarily covering the Sun. These oscillations, if not compensated, they would cause rapid changes in the temperature of the heat transfer fluid, potentially causing turbine damage and unexpected wear. Nevertheless, in order to obtain stable temperatures even in the presence of these phenomena, it was decided to use phase change materials with very high melting temperatures. The use of the PCM's allows to obtain higher values of heat energy, compared to the more conventional ones with sensible heat and allows to operate at more stable temperatures. The decision to integrate it directly into the solar receiver reduces the thermal losses that would otherwise occur in the connecting pipes between both the receiver and the storage tank if they were separated. According to the results which have been found in our research, alloys such as MgSi are well beneficial as a storage material. As a matter of fact, it has excellent thermophysical properties which help to design solar receiver with a great thermal performance as well as higher compactness. Therefore, it will not be influenced by the existence of mechanical stress due to the wind and the excessive shading of the concentrator will be prevented at the same time.

In order to simulate the operation, the most suitable computing methods for this type of system have been investigated and assessed, as well as approaches aimed to achieve good results by lowering the calculation time needed for simulations as much as feasible. The convection losses in our simulation have been considered although the system is set at the time period when the sun is at its highest point. The results are obtained when the device is oriented in a horizontal position in which the hot wall is facing the ground. However, the MGT normally works with a minimal air inlet temperature of 800 °C, based on suitable properties required for a particular application among the common types of PCMs have been shortlisted, we used three of them (MgSi, NiSi and AlSb). In fact, the choice of the PCM is complex, since there is limited data available in the literature for PCMs which melt at temperatures greater than 800 °C. AlSb has shown more prominent results as it could maintain the outlet temperature above 850 °C for a sufficient time period. During the charging phase MgSi showed a rapid melting and remained for about four and half hours with 70%. Based on the results obtained by the simulation, AlSb is observed to be the best suited material to be integrated into the solar receiver because it produced the highest outlet air temperature despite the fact that it had the lowest liquid fraction among the three PCMs, if liquid fraction is to be considered the main factor, MgSi should be selected as the most suitable material for the integration since it had by far the best liquid fraction behavior compared to other two PCMs, as for the NiSi, the liquid fraction behavior was better than that of the AlSb but lower than that of MgSi but it's the least recommended material since it had the lowest outlet air temperature performance. The simulation has been conducted with COMSOL Multiphysics software using irradiance data from the Turin weather station at the Energy Center. Despite the existence of solar radiation changes, the simulations revealed an increase in the operational duration of the system and demonstrated that the temperature of the heat transfer fluid variation was observed. The maximum temperatures which have been obtained were always within the temperature range permitted by the chosen PCM. Thus, it can be used at any geographical location with a significant amount of direct normal irradiance. The incident solar flux of $500(kw/m^2)$ is convenient for the necessary thermal power for MGT which in our study around 32.5 kw, and the maximum temperature obtained in this case is about 1270.3 °C which meets the allowable melting temperature of the cavity material.

5.9 Recommendations and Future Work

Based on the results obtained throughout the work conducted in this thesis; the following is recommended:

- Using lower time-step simulation will produce more accurate results which in turn improves the performance of the system.
- The system can be further enhanced by increasing the air inlet temperature to the solar receiver. Therefore, I suggest to use Mg_2Si as a PCM, due to its ability to maintain higher temperature in a sufficient time period.

For future work; I would suggest:

- Repeating the simulation using different materials than those which are used in this investigation; examples (Fe_2Si_5 , Mg_2Si).
- Repeating the simulation choosing different locations specially those places which have higher DNI such as North Africa and meddle east.
- Investigating the impact of air pressure drop inside the tubes is important parameter which would affect the efficiency of the MGT.
- The velocity and the mass flow rate of the air inside the tubes also play a major role in the design of the system hence we shall take them into consideration for the future research.
- Using different sizes of optical areas with different colors may also be examined for any forthcoming research.

Bibliography

- [1] H. I. Villafán-Vidales, C. A. Arancibia-Bulnes, D. Riveros-Rosas, H. Romero-Paredes, and C. A. Estrada, “An overview of the solar thermochemical processes for hydrogen and syngas production: Reactors, and facilities,” *Renewable and Sustainable Energy Reviews*, vol. 75. Elsevier Ltd, pp. 894–908, 2017. doi: 10.1016/j.rser.2016.11.070.
- [2] M. Liu et al., “Review on concentrating solar power plants and new developments in high temperature thermal energy storage technologies,” *Renewable and Sustainable Energy Reviews*, vol. 53. Elsevier Ltd, pp. 1411–1432, Jan. 01, 2016. doi: 10.1016/j.rser.2015.09.026.
- [3] D. A. Baharoon, H. A. Rahman, W. Z. W. Omar, and S. O. Fadhl, “Historical development of concentrating solar power technologies to generate clean electricity efficiently – A review,” *Renewable and Sustainable Energy Reviews*, vol. 41. Elsevier Ltd, pp. 996–1027, 2015. doi: 10.1016/j.rser.2014.09.008.
- [4] N. Boerema, G. Morrison, R. Taylor, and G. Rosengarten, “High temperature solar thermal central-receiver billboard design,” *Solar Energy*, vol. 97, pp. 356–368, Nov. 2013, doi: 10.1016/j.solener.2013.09.008.
- [5] *Concentrating Solar Power Projects in Italy*. NREL,” www.nrel.gov, Accessed: Jul. 28, 2021. [Online]. Available: [https://www.nrel.gov/csp/solarpaces/by_country_detail.cfm/country = IT](https://www.nrel.gov/csp/solarpaces/by_country_detail.cfm/country=IT)
- [6] “Energy account - Wikipedia.” [https : //it.wikipedia.org/wiki/Conto_energia](https://it.wikipedia.org/wiki/Conto_energia) (accessed Nov. 08, 2021).

- [7] A. G. Fern Andez, J. Gomez-Vidal, E. Or, A. Kruiuzenga, A. Sol E E, and L. F. Cabeza, “Mainstreaming commercial CSP systems: A technology review,” 2019, doi: 10.1016/j.renene.2019.03.049.
- [8] Silvio Toffetti, *Modellazione e Analisi CFD di un Accumulo Termico a Cambiamento di Fase integrato in un Ricevitore Solar*. Supervised by Professors Ing. Davide Papurello, Ing. Massimo Santarelli
- [9] “SunShot Vision Study,” 2010. <https://www.energy.gov/eere/solar/sunshot-vision-study>
- [10] B. Hoffschmidt, S. Alexopoulos, J. Götttsche, M. Sauerborn, and O. Kaufhold, “High concentration solar collectors,” in *Comprehensive Renewable Energy*, vol. 3, Elsevier Ltd, 2012, pp. 165–209. doi: 10.1016/B978-0-08-087872-0.00306-1.
- [11] Z. Jin, Y. Hui, R. Ayyanar, and A. Rodriguez, “Concentrated Solar Power Generation by the Graduate Supervisory Committee,” 2013.
- [12] “Archimede Solar Energy.” http://www.archimedesolarenergy.it/solar_receiver_tube.htm (accessed Jul. 28, 2021).
- [13] Q. Chen, Y. Wang, J. Zhang, and Z. Wang, “The knowledge mapping of concentrating solar power development based on literature analysis technology,” *Energies*, vol. 13, no. 8, Apr. 2020, doi: 10.3390/en13081988.
- [14] M. T. Islam, N. Huda, A. B. Abdullah, and R. Saidur, “A comprehensive review of state-of-the-art concentrating solar power (CSP) technologies: Current status and research trends,” *Renewable and Sustainable Energy Reviews*, vol. 91. Elsevier Ltd, pp. 987–1018, Aug. 01, 2018. doi: 10.1016/j.rser.2018.04.097.
- [15] S. Guarino, A. Buscemi, G. Ciulla, M. Bonomolo, and V. lo Brano, “A dish-stirling solar concentrator coupled to a seasonal thermal energy storage system in the southern mediterranean basin: A cogenerative layout hypothesis,” *Energy Conversion and Management*, vol. 222, Oct. 2020, doi: 10.1016/j.enconman.2020.113228.
- [16] F. Wirtschaftswissenschaft, R. Tol, and H. Wenzlawski, “The global CSP market-its industry, structure and decision mechanisms Diplomarbeit.”

- [17] U. Zimmermann, L. Keppler, and N. Kenya, “Terminal Evaluation: UN Environment/Global Environment Facility Project ‘Seed Capital Assistance Facility, Phase I (Renewable Energy Enterprise Development)’ (GEF project ID 1609) Evaluation Office of UN Environment,” 2018.
- [18] “CSP energy storage may provide stable, scalable and reliable power.” *https://www.power-technology.com/comment/csp-energy-storage/* (accessed Aug. 22, 2021).
- [19] U. Pelay, L. Luo, Y. Fan, D. Stitou, and M. Rood, “Thermal energy storage systems for concentrated solar power plants,” *Renewable and Sustainable Energy Reviews*, vol. 79. Elsevier Ltd, pp. 82–100, 2017. doi: 10.1016/j.rser.2017.03.139.
- [20] D. Yadav and R. Banerjee, “A review of solar thermochemical processes,” *Renewable and Sustainable Energy Reviews*, vol. 54. Elsevier Ltd, pp. 497–532, Feb. 01, 2016. doi: 10.1016/j.rser.2015.10.026.
- [21] J. Cot-Gores, A. Castell, and L. F. Cabeza, “Thermochemical energy storage and conversion: A-state-of-the-art review of the experimental research under practical conditions,” *Renewable and Sustainable Energy Reviews*, vol. 16, no. 7. pp. 5207–5224, Sep. 2012. doi: 10.1016/j.rser.2012.04.007.
- [22] P. Pardo, A. Deydier, Z. Anxionnaz-Minvielle, S. Rougé, M. Cabassud, and P. Cognet, “A review on high temperature thermochemical heat energy storage,” *Renewable and Sustainable Energy Reviews*, vol. 32. pp. 591–610, Apr. 2014. doi: 10.1016/j.rser.2013.12.014.
- [23] A. Palacios, C. Barreneche, M. E. Navarro, and Y. Ding, “Thermal energy storage technologies for concentrated solar power – A review from a materials perspective,” *Renewable Energy*, vol. 156. Elsevier Ltd, pp. 1244–1265, Aug. 01, 2020. doi: 10.1016/j.renene.2019.10.127.
- [24] K. G. Sakellariou, G. Karagiannakis, Y. A. Criado, and A. G. Konstandopoulos, “Calcium oxide based materials for thermochemical heat storage in concentrated solar power plants,” *Solar Energy*, vol. 122, pp. 215–230, Dec. 2015, doi: 10.1016/j.solener.2015.08.011.

- [25] M. Liu et al., “Review on concentrating solar power plants and new developments in high temperature thermal energy storage technologies,” *Renewable and Sustainable Energy Reviews*, vol. 53. Elsevier Ltd, pp. 1411–1432, Jan. 01, 2016. doi: 10.1016/j.rser.2015.09.026.
- [26] T. Xiong, Y. Wang, and X. Yang, “Numerical investigation of dynamic melting process in a thermal energy storage system using U-tube heat exchanger,” *Advances in Mechanical Engineering*, vol. 9, no. 5, May 2017, doi: 10.1177/1687814017707415.
- [27] G. Ragnolo, L. Aichmayer, W. Wang, T. Strand, and B. Laumert, “Technoeconomic Design of a Micro Gas-turbine for a Solar Dish System,” in *Energy Procedia*, May 2015, vol. 69, pp. 1133–1142. doi: 10.1016/j.egypro.2015.03.182.
- [28] M. A. Bashir, A. Giovannelli, and H. M. Ali, “Design of high-temperature solar receiver integrated with short-term thermal storage for Dish-Micro Gas Turbine systems,” *Solar Energy*, vol. 190, pp. 156–166, Sep. 2019, doi: 10.1016/j.solener.2019.07.077.
- [29] A. Giovannelli, M. A. Bashir, and E. M. Archilei, “High-temperature solar receiver integrated with a short-term storage system,” in *AIP Conference Proceedings*, Jun. 2017, vol. 1850. doi: 10.1063/1.4984405.
- [30] M. A. Bashir, A. Giovannelli, K. P. Amber, M. S. Khan, A. Arshad, and A. M. Daboo, “High-temperature phase change materials for short-term thermal energy storage in the solar receiver: Selection and analysis,” *Journal of Energy Storage*, vol. 30, Aug. 2020, doi: 10.1016/j.est.2020.101496.
- [31] M. A. Bashir and A. Giovannelli, “Design optimization of the phase change material integrated solar receiver: A numerical parametric study,” *Applied Thermal Engineering*, vol. 160, Sep. 2019, doi: 10.1016/j.applthermaleng.2019.114008.
- [32] “Turin climate: Average Temperature, weather by month, Turin weather averages - Climate-Data.org.” <https://en.climate-data.org/europe/italy/piemont/turin-1108/> (accessed Oct. 29, 2021).
- [33] B. R. Munson, T. H. Okiishi, W. W. Huebsch, Rothmayer, and A. P, *Fundamentals of fluid mechanics*. 2013.